Research Square

Preprints are preliminary reports that have not undergone peer review.
They should not be considered conclusive, used to inform clinical practice,
or referenced by the media as validated information.

Integrative Network Pharmacology, Molecular Dynamics, and Multi-Level Molecular Validation of Moringa oleifera-Derived Bioactive Compounds Against Prostate Cancer

Supriya Maurya
University of Allahabad
Saba Ehsan
University of Allahabad
Anupriya Chaudhry
University of Allahabad
Prof. Mohan P. Singh
mpsingh.16@gmail.com
University of Allahabad

Research Article

Keywords: Moringa oleifera, prostate cancer, network pharmacology, molecular docking, molecular dynamics simulation, hub genes, immune infiltration, computational drug discovery

Posted Date: November 24th, 2026

DOI: https://doi.org/10.21203/rs.3.rs-11839686/v1

License: This work is licensed under a Creative Commons Attribution 4.0 International License.
Read Full License

Additional Declarations: The authors declare no competing interests.

Integrative Network Pharmacology, Molecular Dynamics, and Multi-Level Molecular Validation of Moringa oleifera-Derived Bioactive Compounds Against Prostate Cancer

Abstract

Prostate cancer (PCa) remains a main health challenge, highlighting the essential to recognize bioactive compounds and molecular targets for further therapeutic investigation. This study presents an integrated computational framework to investigate the potential anticancer relevance of *Moringa oleifera*-derived compounds against PCa by combining network pharmacology, molecular docking, molecular dynamics (MD) simulations, and multi-level molecular and clinical data analyses. Five phytoconstituents were prioritized through drug-likeness and predicted pharmacokinetic screening. Target prediction identified 8,841 compound-associated targets, which were compared with 452 PCa-associated genes, revealing 253 overlapping targets. Protein–protein interaction analysis and functional enrichment highlighted interconnected networks associated with inflammation, apoptosis, immune regulation, and cancer-related signalling. The top 10 hub genes were TNF, NFKB1, HIF1A, PTGS2, JUN, IL1B, IFNG, CASP3, IL1A, and TLR4. Molecular docking identified a binding score of −7.3 kcal/mol for CID 12366 against the 5F19 protein structure, compared with −8.6 kcal/mol for CID 9821849. Subsequent 200-ns MD simulations revealed differences in structural deviation, residue flexibility, and hydrogen-bond formation, whereas the reported radius of gyration and solvent-accessible surface area suggested broadly comparable compactness and solvent exposure. External analyses further examined gene expression, prognostic associations, protein expression, promoter methylation, and immune-cell infiltration, identifying potential clinical relevance for selected hub genes. The novelty of this study lies in integrating compound prioritization, network-based target identification, structural dynamics, and independent molecular and clinical evidence within a unified PCa-focused workflow. Experimental validation, verification of trajectory metrics, and binding free-energy calculations are required to establish the biological significance of the prioritized candidates.

Keywords: *Moringa oleifera*; prostate cancer; network pharmacology; molecular docking; molecular dynamics simulation; hub genes; immune infiltration; computational drug discovery.

1. Introduction

Prostate cancer (PCa) is one of the furthermost recurrently established malignancies in men and remnants a major global health concern. Its progression comprises interrelated molecular processes, including androgen signalling, dysregulated cell proliferation, apoptosis, inflammation, metabolic adaptation, and tumour–microenvironment interactions (Militaru et al., 2023). In spite of developments in androgen-deprivation therapy, androgen receptor pathway inhibitors, chemotherapy, and targeted treatments, therapeutic resistance and disease progression remain significant challenges, predominantly in progressive disease (Harris et al., 2009). These limitations highlight the essential to classify candidate bioactive molecules and examine their probable interactions with molecular targets occupied in prostate cancer. Computational approaches can facilitate this process by integrating chemical, molecular, and clinical data, though their predictions require experimental validation (Maurya et al., 2026).

Natural products characterize an important source of structurally diverse compounds with potential pharmacological activities. *Moringa oleifera* Lam. (Moringaceae) has involved significant attention because of its reported nutritional, antioxidant, anti-inflammatory, and anticancer properties (Chaudhary et al., 2026). Its phytochemical composition includes flavonoids, phenolic compounds, glucosinolates, isothiocyanates, sterols, and fatty-acid derivatives. However, phytochemical abundance and biological activity depend on the plant part, extraction method, and analytical conditions. Furthermore, findings attained from crude extracts cannot necessarily be accredited to individual ingredients or generalized across different cancer models (Divya et al., 2024). Therefore, systematic compound prioritization and molecular target identification are important for investigation the potential significance of *M. oleifera*-derived compounds to prostate cancer.

Previous studies have investigated the anticancer properties of *M. oleifera* through phytochemical characterization, network pharmacology, and experimental assessment of cancer-associated cellular processes (Singh et al., 2025). Network-based investigations of its leaf-derived compounds have explored potential molecular targets and cancer-related signalling pathways, whereas experimental studies in PC3 prostate cancer cells have inspected extract-associated molecular and epigenetic changes (Muazzam, 2021). These investigations provide a foundation for further research; however, differences in plant material, compound composition, and analytical strategy limit direct comparisons between their findings. Importantly, evidence of extract-associated cellular effects does not establish the binding affinity, pharmacokinetic suitability, or dynamic stability of individual phytochemicals (Rombolà et al., 2020). An combined compound-to-target investigation is consequently warranted to connect candidate selection with molecular network organization, structural interaction analysis, and independent prostate cancer datasets. Network pharmacology delivers a systems-level approach to identifying shared compound-associated and disease-associated targets, while protein–protein interaction (PPI) networks and Gene Ontology (GO) and Kyoto Encyclopedia of Genes and Genomes (KEGG) enrichment analyses help characterize their functional relationships (Maurya et al., 2026). Nevertheless, network centrality and pathway enrichment alone cannot establish direct target engagement or causal mechanisms. Molecular docking can predict reasonable ligand–protein binding poses, and molecular dynamics (MD) simulations can assess the conformational behaviour of selected complexes over time (Salmaso & Moro, 2018). Complementary analyses of gene expression, survival associations, protein expression, promoter methylation, and immune-cell infiltration can further contextualize the biological relevance of prioritized targets. Integrating these approaches delivers a broader computational assessment, though the resulting evidence remains hypothesis-generating rather than proof of therapeutic efficacy (Bayram et al., 2026).

In the present study, *M. oleifera*-derived bioactive compounds were prioritized using phytochemical information and predicted drug-likeness and pharmacokinetic properties. Their potential molecular targets were intersected with prostate cancer-associated genes, followed by PPI network construction, functional-module identification, hub-gene prioritization, and GO and KEGG enrichment analyses. Selected hub proteins were afterward appraised by molecular docking, using abiraterone acetate as the reference drug, followed by 200-ns MD simulations

to investigate structural deviation, residue flexibility, radius of gyration, hydrogen-bond formation, and solvent-accessible surface area. The prioritized targets were further examined using gene-expression, prognostic, protein-expression, promoter-methylation, and immune-infiltration datasets.

The novelty of this study lies in integrating compound-level screening, network-based target prioritization, structure-based interaction analysis, long-timescale MD simulations, and complementary molecular and clinical data interrogation within a single prostate cancer-focused computational workflow. Rather than presumptuous well-known anticancer activity, this method aims to prioritize candidate compounds, characterize their predicted interactions with selected targets, and investigate the relevance of these targets to prostate cancer-associated molecular and clinical features. The discoveries may distribute a rational basis for selecting candidates for succeeding biochemical, cellular, and pharmacological validation.

Material and methods

Identification of moringa-derived bioactive compounds and prediction of their biological targets

A total of 20 compounds were recognized through GC–MS analysis of Moringa oleifera gum (Chaudhary et al., 2026), and eight phytoconstituents were shortlisted based on relative peak area (≥1%, with compounds near the threshold [≥0.9%] reserved when supported by biological relevance), after removing duplicates and potential analytical artifacts; these compounds were additional estimated using SwissADME for drug-likeness and predicted pharmacokinetic properties, including ≤1 Lipinski rule violation, high gastrointestinal absorption, and a bioavailability score ≥0.55, resulting in the selection of five bioactive compounds and 1 reference/control compounds for subsequent molecular docking analysis, with their projected binding interactions compared to measure their relative potential against the selected molecular target all provided in supplementary table 1.

Access to Potential Molecular Targets of Moringa oleifera

Potential molecular targets of the shortlisted *Moringa oleifera*–derived bioactive compounds were projected using their PubChem compound identifiers (CIDs), canonical SMILES, or SDF structures retrieved from PubChem **https://pubchem.ncbi.nlm.nih.gov/**. Target prediction was accomplished using DIGEP-Pred (http://www.way2drug.com/ge/ and SuperPred **https://prediction.charite.de/**, applying the respective screening criteria of a prediction score greater than 0.5 for DIGEP-Pred and a probability score greater than 80 for SuperPred, as detailed by the respective platforms (He et al., 2023); (Khanal et al., 2022);(Desai et al., 2025) . The predicted protein targets were mapped to their corresponding gene symbols using UniProt (UniProt Consortium, 2018), and the resulting gene lists were merged and deduplicated to get

a non-redundant set of potential molecular targets for succeeding network pharmacology and functional enrichment analyses.

Identification of Prostate Cancer-Associated Targets

Prostate cancer (PCa)-associated genes were retrieved from GeneCards https://www.**genecards**.org/ , Online Mendelian Inheritance in Man (OMIM) **https://www.omim.org/** , and PharmGKB (**https://www.pharmgkb.org/**) using "prostate cancer" as the search term (Zhong et al., 2022); (Hou et al., 2022);(Jia et al., 2024). Genes retrieved from GeneCards were filtered using a relevance score greater than 30, while disease-associated targets from the other databases were composed according to their available annotations. Protein and target names were standardized to official gene symbols using UniProt, and duplicate entries were removed to generate a non-redundant set of PCa-associated targets (Li et al., 2025). Finally, the predicted targets of the shortlisted Moringa oleifera–derived bioactive compounds were interconnected with the PCa-associated gene set to recognize common targets potentially tangled in the anticancer effects of the selected compounds. These overlapping targets were reserved for subsequent protein–protein interaction (PPI) network construction, hub-gene identification, and functional enrichment analyses (Sharma et al., 2025).

Identification of Overlapping Targets Between Compounds and Disease

The predicted molecular targets of the shortlisted Moringa oleifera–derived bioactive compounds were intersected with the prostate cancer (PCa)-associated disease targets using Venny 2.1.0 (https://bioinfogp.cnb.csic.es/tools/venny/index.html) (Gupta et al., 2026). The overlapping genes were recognized to control the common molecular targets communal by the bioactive compounds and PCa, providing insights into their potential target-associated anticancer mechanisms (Xu et al., 2026). These common targets were considered potential therapeutic targets of Moringa oleifera against PCa and were then used for protein–protein interaction network construction, hub-gene identification, and functional enrichment analysis (Hazarika et al., 2025).

PPI Network Construction and Core Target Screening

The protein–protein interaction (PPI) network of the overlapping targets associated with *Moringa oleifera*–derived bioactive compounds and prostate cancer (PCa) was constructed using the STRING database (https://string-db.org/) with a high-confidence interaction score

threshold of ≥0.7 (Szklarczyk et al., 2025). The interaction data were exported in tab-separated values (TSV) format and imported into Cytoscape v3.9.1 for network visualization and topological analysis (Shannon et al., 2003)**.** Densely connected functional modules were first identified using the Molecular Complex Detection (MCODE) plugin by analysing the whole network with the following parameters: degree cutoff = 2, node score cutoff = 0.2, K-core = 2, and maximum depth = 100, with the haircut option enabled and the fluff and include loops options disabled (Bader & Hogue, 2003)**.** Clusters were ranked by MCODE score, and the highest-scoring cluster was considered the key functional module. Subsequently, hub genes were identified using the Maximal Clique Centrality (MCC) algorithm of the cytoHubba plugin, and the top 10 ranked nodes were selected as core targets (Chin et al., 2014)**.** The MCC-derived hub genes were then associated with the genes of the top MCODE cluster to describe overlapping, high-confidence core targets, which were selected for succeeding functional enrichment and molecular docking analyses.

Gene Ontology (GO) and KEGG pathway enrichment examination

ShinyGO 0.7 was used to achieve Gene Ontology (GO) and Kyoto Encyclopedia of Genes and Genomes (KEGG) pathway enrichment analyses (http://bioinformatics.sdstate.edu/go/) (Ehsan et al., 2026). Gene Ontology offers a standardized, computationally accessible framework for describing gene functions across three categories: biological process (BP), molecular function (MF), and cellular component (CC) (Botstein et al., 2000). KEGG was used as a reference knowledge base to classify enriched biological pathways and interpret the functional relationships among the selected genes (Du et al., 2014). Pathways and GO terms with $p \leq 0.05$ were considered statistically significant. The enrichment results were visualized using a dot plot with the following parameters: x-axis: fold enrichment; dot colour: $-\log_{10}$(FDR), with red representing higher values and blue representing lower values; dot size: number of genes associated with each enriched term; aspect ratio: 2; and plot theme: default. The dot plot was used to facilitate comparison of enrichment magnitude, statistical significance, and gene representation across enriched biological processes and pathways (Kumar et al., 2024).

Core Target Screening

Core targets within the protein–protein interaction (PPI) network was recognized using the cytoHubba plugin in Cytoscape v3.9.0. Four topological algorithms—Degree, Maximum Neighborhood Component (MNC), Maximal Clique Centrality (MCC), and Closeness centrality—were applied independently to rank the network nodes, and the top 10 targets from

each method were selected (W. Ahmed et al., 2025). The overlapping targets identified across all four ranking methods were considered core hub genes, representing highly connected and topologically significant nodes within the PPI network (M. M. Ahmed et al., 2022). These core targets were ordered for succeeding functional enrichment analysis and molecular docking to explore their probable characters in the anticancer activity of Moringa oleifera–derived bioactive compounds in contradiction of prostate cancer.

Molecular Docking, Analysis, and Visualization

Molecular docking was accomplished to estimate the binding affinities of Moringa-derived bioactive compounds against the top 10 prostate cancer (PC)-associated hub targets prioritized using MCC centrality analysis of the protein–protein interaction network. Abiraterone acetate, an FDA-approved anticancer drug, was used as a reference control for comparative docking analysis. Ligand structures were retrieved from PubChem in SDF format and transformed to PDBQT using Open Babel v2.4.1. Protein structures were attained from the RCSB Protein Data Bank (PDB), prepared using BIOVIA Discovery Studio Visualizer 2021 by removing water molecules and co-crystallized ligands, and supplemented with polar hydrogens (Ehsan,et al., 2026; Maurya et al., 2026). The prepared protein structures were converted to PDBQT format using AutoDock Tools v1.5.7 (Chaudhary et al., 2026; Ehsan et al., 2026). Molecular docking was subsequently accomplished using AutoDock Vina v1.2.5, with grid boxes well-defined to encompass the target binding sites and classify favourable ligand-binding poses. The resulting docking scores were compared to prioritize potential lead compounds. Docked protein–ligand complexes were visualized using BIOVIA Discovery Studio Visualizer 2021 to examine binding poses and intermolecular interactions (Nivatya et al., 2025). Two-dimensional interaction diagrams were engendered to characterize interactions, including hydrogen bonds, hydrophobic contacts, van der Waals interactions, and π-alkyl interactions, where present.

Molecular Dynamics (MD) Simulation

Molecular dynamics (MD) simulations were achieved using GROMACS (version 2023) with the CHARMM36 force field under periodic boundary conditions to examine the structural stability and dynamic behaviour of the protein–ligand complex acknowledged through molecular docking (Grewal et al., 2025). The ligand topology and force-field parameters for isosorbide were engendered using the SwissParam server to guarantee compatibility with the CHARMM force field. The protein–ligand complex was placed in a cubic simulation box, solvated using the TIP3P water model, and neutralized by adding appropriate counterions.

Energy minimization was accomplished using the steepest descent algorithm, followed by the conjugate gradient method, to relieve steric clashes and improve the system geometry. The system was subsequently equilibrated underneath constant-volume (NVT) and constant-pressure (NPT) ensembles to stabilize the temperature and pressure before production dynamics (Yadav & Padhi, 2025).

The production MD simulation was directed for 200 ns using a 2 fs integration time step at 300 K under periodic boundary conditions. Trajectory coordinates were recorded at regular intervals for subsequent structural and dynamic analyses. The stability of the protein–ligand complex was evaluated by calculating the root-mean-square deviation (RMSD), root-mean-square fluctuation (RMSF), radius of gyration (Rg), and solvent-accessible surface area (SASA). Hydrogen-bond analysis was also accomplished to inspect the perseverance of ligand–protein interactions throughout the simulation. Collectively, these analyses were used to assess conformational stability, residue-level flexibility, protein compactness, solvent exposure, and the maintenance of key binding interactions over the 200 ns trajectory (Bouamri et al., 2026).

External validation of core targets

.1 Gene expression levels of core targets

In the "Expression DIY" of GEPIA (**http://gepia.cancer-pku.cn/**), the mRNA expression levels and pathological stages of the core targets were verified (Deng et al., 2023). |log2FC|Cutoff:1, *p*-value Cutoff:0.01.

Analysis of the Prognostic Significance of Hub Genes in Prostate Cancer

The prognostic significance of the selected hub genes in prostate adenocarcinoma (PRAD) was evaluated using the Kaplan–Meier Plotter (KM Plotter; http://kmplot.com/analysis/) (Gao et al., 2025). Overall survival (OS) and other available survival endpoints were evaluated according to the expression levels of the selected genes: TNF, NFKB1, HIF1A, PTGS2, JUN, IL1B, IFNG, CASP3, IL1A, and TLR4. Kaplan–Meier survival curves were generated to compare patient groups with high and low gene expression, and statistical significance was evaluated using the log-rank test. Hazard ratios (HRs) and corresponding 95% confidence intervals (CIs), where available, were recorded to assess the association between gene expression and patient outcomes (Nagy et al., 2021). The prognostic results were understood to recognize hub genes possibly accompanying with survival in PRAD.

Protein Expression Levels of Core Targets

To validate the protein expression patterns of the identified hub genes in prostate cancer (PRAD), protein expression data were examined using the Human Protein Atlas database (https://www.proteinatlas.org/) (Liu et al., 2022a). The protein expression profiles of the designated core targets in prostate cancer tissues were associated with those in normal prostate tissues. This analysis designed to assess the protein-level expression patterns of the hub targets and provide complementary evidence for their potential participation in prostate cancer progression. The protein expression findings were measured alongside the mRNA expression profiles to support the biological relevance of the identified targets (Rajadnya et al., 2024).

Protein expression analysis of hub genes

Protein expression levels of the ten prostate cancer (PRAD)-associated hub genes were investigated using the Human Protein Atlas (HPA) database Protein expression levels of the ten prostate cancer (PRAD)-associated hub genes were inspected using the Human Protein Atlas (HPA) database (Liu et al., 2022b). Immunohistochemistry (IHC) data were inspected to measure the protein expression patterns of TNF, NFKB1, HIF1A, PTGS2, JUN, IL1B, IFNG, CASP3, IL1A, and TLR4 in normal prostate and prostate cancer tissues. This analysis meant to deliver protein-level evidence to complement the transcriptomic findings and estimate the expression patterns of the selected hub genes at the tissue level.

.2 Immune Cell Infiltration of Core Targets

To examine the relationship between the recognized hub genes and the tumour immune microenvironment in prostate cancer (PRAD), the TIMER database was used to appraise the relations between the expression levels of the top 10 core targets (TNF, NFKB1, HIF1A, PTGS2, JUN, IL1B, IFNG, CASP3, IL1A, and TLR4) and immune cell infiltration. The analysis absorbed on major immune cell populations, including B cells, $CD4^+$ T cells, $CD8^+$ T cells, neutrophils, macrophages, and dendritic cells. This calculation designed to discover the possible participation of the identified hub genes in immune regulation and tumour–immune interactions in prostate cancer. The detected associations were understood to control whether the expression of individual hub genes was correlated with variations in immune cell infiltration (Long et al., 2020).

Result

Identification of Moringa oleifera-Derived Bioactive Compounds and Prediction of Their Biological Targets

A total of 20 bioactive compounds derived from Moringa oleifera were recognized through a comprehensive literature survey of previously published studies examining its phytochemical composition and biological activities (Chaudhary et al., 2026). After filtration of biological activities 8 compounds are gain provided in supplementary table 2. The canonical SMILES notations of the identified compounds were retrieved from PubChem and subsequently used for drug-likeness and pharmacokinetic evaluation using the SwissADME web tool. Among the 20 selected compounds, five seen the predefined screening criteria, together with zero or one violation of Lipinski's Rule of Five, a molecular weight of 150–500 g/mol, a topological polar surface area (TPSA) of 20–130 Å², and satisfactory projected pharmacokinetic properties, including CYP2D6 and CYP3A4 inhibition profiles and blood–brain barrier permeability. The five shortlisted compounds were subsequently selected for further investigation of their potential molecular targets and possible relevance to prostate cancer (Table 1).

Table 1: Drug-likeness and Pharmacokinetic Properties of the Selected Bioactive Compounds

		Physiochemical properties								Pharmacokinetics		
S. No.	**Compounds / PubChem ID**	**MW (g/mol)**	**H-Bond Acceptors**	**H-Bond Donors**	**MLOGP**	**TPSA (Å²)**	**Rotatable Bonds**	**Lipinski's Violations**	**Bioavailability Score**	**BBB**	**CYP2D6**	**CYP3A4**
1	Benzo[b]thiophene (7221)	134.20	0	0	2.64	28.24	0	0	0.55	No	No	No
2	Hexadecanoic acid, methyl ester (8181)	270.45	2	0	4.44	26.30	15	1	0.55	No	No	No
3	Hexadecanoic acid, ethyl ester (12366)	284.48	2	0	4.67	26.30	16	1	0.55	No	No	No
4	n-Hexadecanoic acid (985)	256.42	2	1	4.19	37.30	14	1	0.85	No	No	No
5	Tetradecanoic acid (11005)	228.37	2	1	3.69	37.30	12	0	0.85	No	No	No

Target for moringa and prostate cancer Target Identification of Moringa oleifera Against Prostate Cancer

After implementation ADME profiling, the potential targets of Moringa oleifera bioactive compounds were projected using SwissTargetPrediction, SuperPred, and DIGEP-Pred, resulting in 8,841 predicted targets. To classify genes associated with prostate cancer, GeneCards, DisGeNET, and OMIM were scientifically queried, yielding 452 disease-related genes. Comparative analysis of these two target sets revealed 253 shared genes, representing potential molecular links between M. oleifera bioactive compounds and prostate cancer. These overlapping targets are offered in the Venn diagram (Fig. 1).

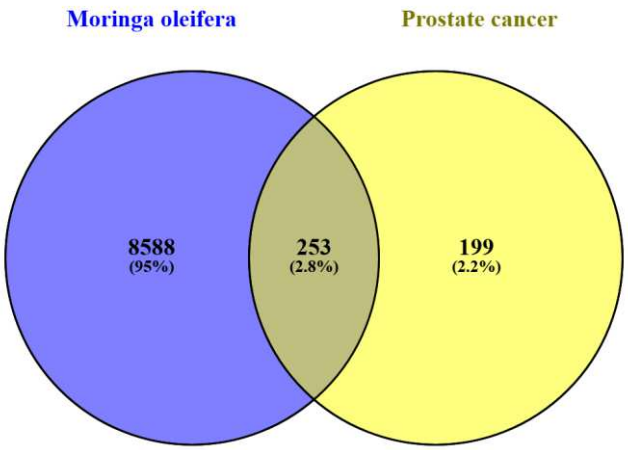


Figure 1. Venn diagram illustrating the overlap between Moringa oleifera-associated targets and prostate cancer-associated genes. A total of 253 shared genes were identified between the two datasets, while 8,588 genes were unique to M. oleifera and 199 genes were specific to prostate cancer. The overlapping genes were selected for subsequent analyses to identify potential therapeutic targets and investigate the molecular mechanisms underlying the anticancer potential of M. oleifera.

Protein–Protein Interaction (PPI) Network Construction and Analysis

The PPI network of the overlapping targets, created using STRING (confidence score ≥0.7) and visualised in Cytoscape, comprised 188 nodes and 1,528 edges in a single connected component (Fig. 2[A]), with an average of 16.255 neighbours per node, a network diameter of

5, a radius of 3, a characteristic path length of 2.416, a clustering coefficient of 0.485, a network density of 0.087, and a network centralization of 0.388, indicating that the targets are functionally interconnected. MCODE analysis of the entire network recognized several clusters, amongst which the top-ranked cluster (Cluster 1) had an MCODE score of 26.375 and contained 33 nodes and 422 edges (Fig. 2[B]). After this cluster showed an average of 25.576 neighbours per node, a diameter of 2, a radius of 1, a characteristic path length of 1.201, a clustering coefficient of 0.868, and a density of 0.799, indicating a very tightly connected module. In addition to the hub genes designated below, it encompassed other inflammation-, apoptosis-, and survival-related genes such as NOS2, HMOX1, CASP8, CASP9, MTOR, MDM2, and ERBB2 (all 33 genes with their MCODE node scores are enumerated in Supplementary Table 3). The remaining clusters were small (MCODE score 2.5–3.0; 3–11 nodes) and were not analysed further. Using the MCC algorithm of cytoHubba, the top 10 hub genes were recognized as TNF, NFKB1, HIF1A, PTGS2, JUN, IL1B, IFNG, CASP3, IL1A, and TLR4 (Fig. 2[C]), which are connected with inflammation, immune response, hypoxia signalling, and apoptosis. Remarkably, all 10 MCC hub genes were positioned within Cluster 1, viewing that they occupy the topological core of the network, and this agreement between two autonomous algorithms cares their selection as core targets for enrichment and docking analyses.

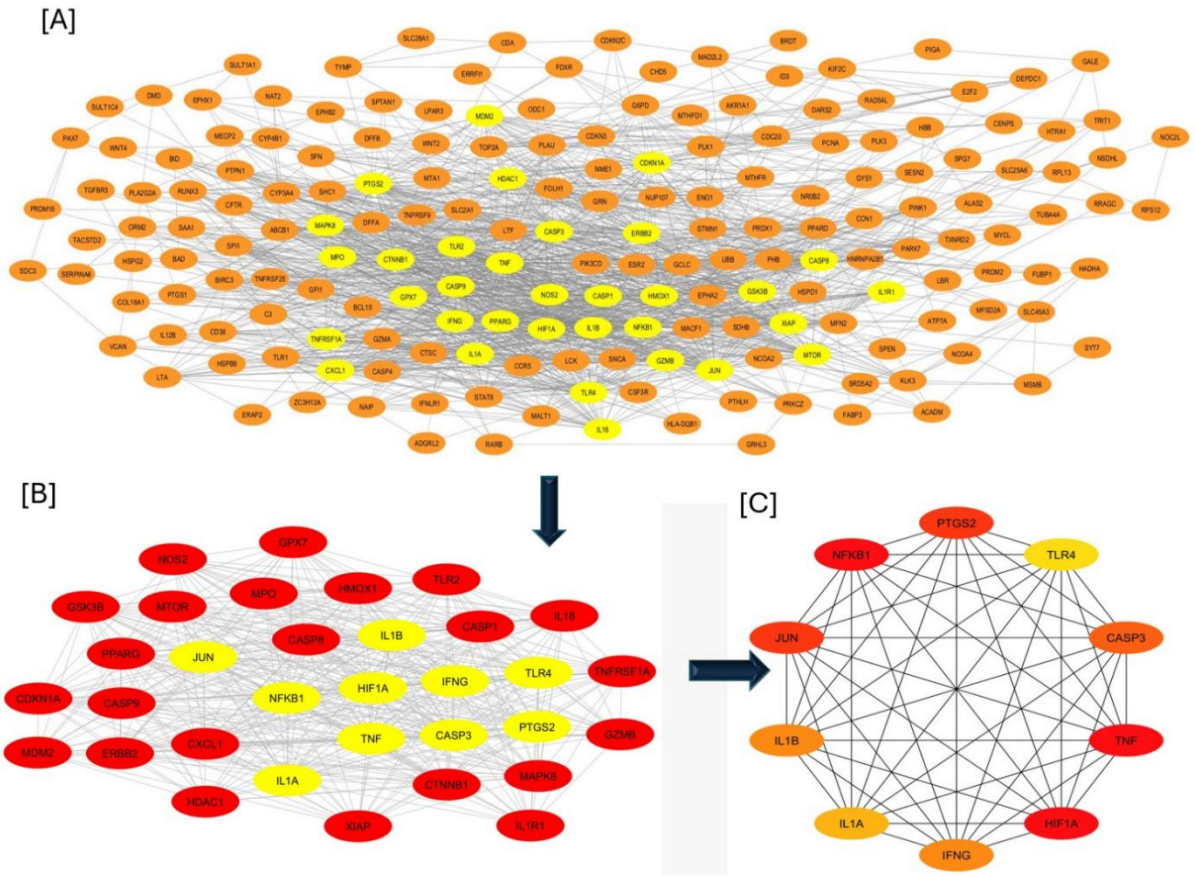


Figure 2: PPI network of the top 10 hub genes based on degree centrality analysis. Nodes represent proteins, while edges represent protein–protein interactions.

Results of GO and KEGG enrichment analysis

Gene Ontology (GO) enrichment analysis was accomplished to examine the biological functions of the overlapping target genes across three major categories: biological process (BP), cellular component (CC), and molecular function (MF). As shown in Fig. 3, the BP analysis exposed significant enrichment in apoptotic signalling, regulation of apoptosis, cellular responses to chemical stimuli, programmed cell death, regulation of cell proliferation, and responses to stress. These discoveries advocate that the acknowledged targets may be involved in the regulation of cell survival, apoptosis, and stress-responsive mechanisms. The CC analysis showed enrichment in transcription repressor complexes, mitochondrial membranes, cell surfaces, chromatin, extracellular exosomes, extracellular vesicles, and plasma membrane-bound cellular projections. The MF analysis emphasized NAD^+-nucleosidase activity, peroxidase activity, antioxidant activity, oxidoreductase activity, DNA-binding transcription factor activity, protein kinase binding, and transcription coregulator

activity, indicating potential roles in transcriptional regulation, redox homeostasis, and intracellular signalling shown in fig 3.

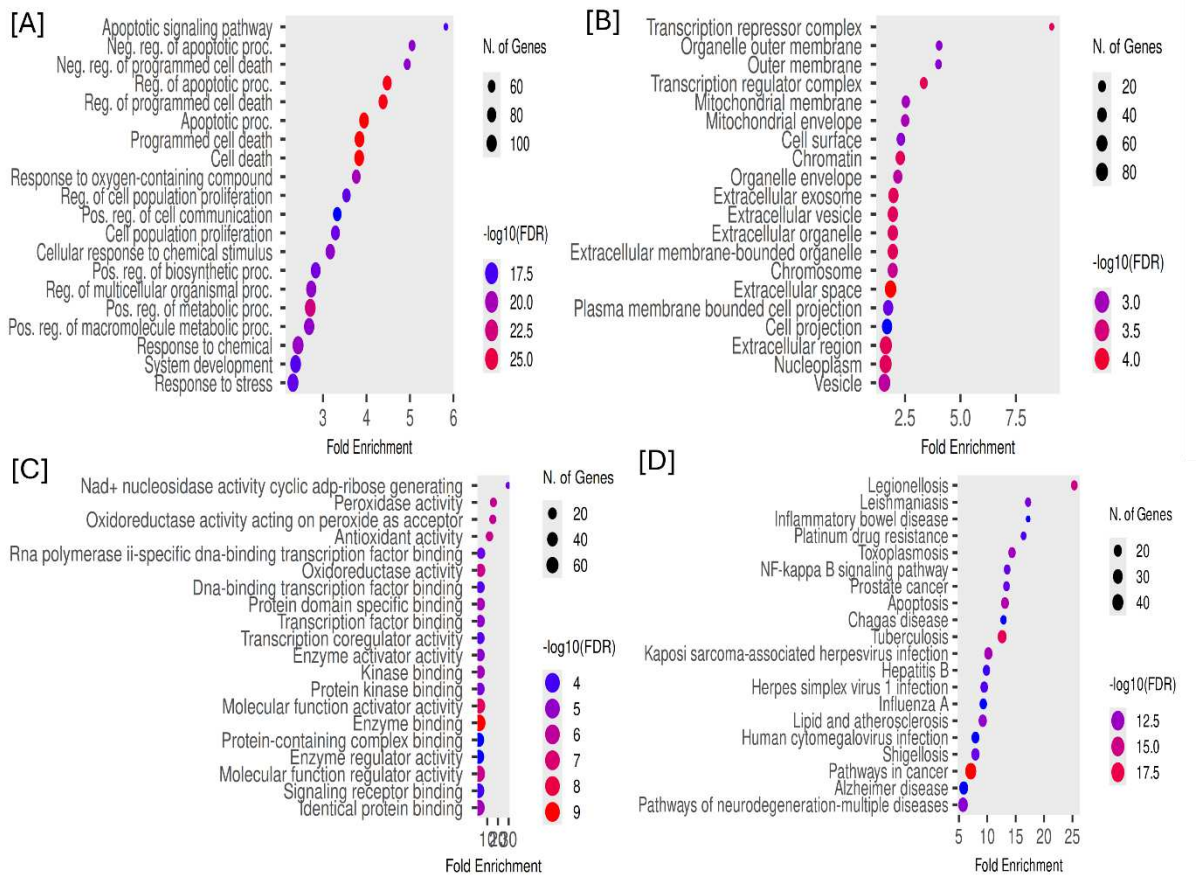


Figure 3: Gene Ontology (GO) and KEGG pathway enrichment analysis of the overlapping target genes. The dot plots illustrate enriched biological processes, cellular components, molecular functions, and KEGG pathways based on fold enrichment, gene counts, and −log10(FDR).

Further, KEGG pathway enrichment analysis exposed associations with several cancer-related and inflammation-associated pathways, including the NF-kappa B signalling pathway, apoptosis, pathways in cancer, and pathways involved in neurodegeneration and infectious diseases. Amongst these, the NF-kappa B signalling pathway and apoptosis are predominantly relevant to inflammatory regulation and cell death, respectively. The enrichment of pathways in cancer further supports the potential involvement of the overlapping targets in cancer-associated molecular processes. The dot plots characterize fold enrichment, the number of genes associated with each term, and statistical significance expressed as −log10(FDR), with larger and more forcefully coloured dots illustrative greater gene representation and stronger enrichment significance, respectively.

Overall, the GO and KEGG enrichment results specify that the recognized targets are associated with interconnected biological processes involving apoptosis, inflammation, transcriptional regulation, oxidative stress, and cancer-related signalling. These discoveries provide functional insights into the potential molecular mechanisms underlying the investigated biological condition and support further investigation of the enriched pathways and their associated hub genes presented in Fig 4.

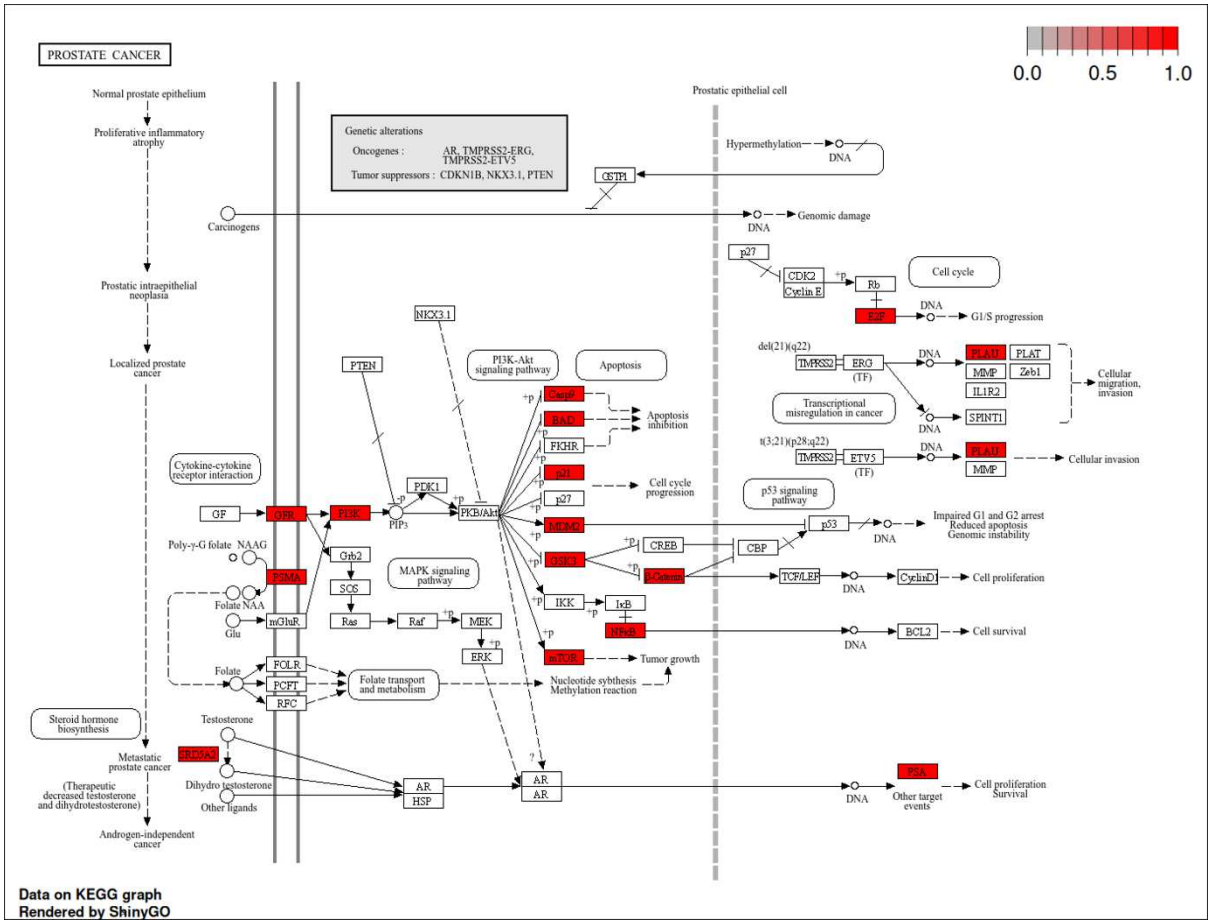


Figure 4. KEGG pathway mapping of prostate cancer. The prostate cancer pathway was visualized using ShinyGO, highlighting genes associated with key oncogenic signalling pathways and cellular processes. Red-highlighted nodes represent genes from the submitted gene set mapped to the pathway. The diagram demonstrates their involvement in pathways regulating cell-cycle progression, apoptosis, PI3K–AKT signalling, tumour growth, cellular proliferation, and survival.

Molecular docking analysis and lead compound prioritization

Molecular docking was achieved to assess the binding potential of six selected compounds (PubChem CIDs: 11005, 7221, 8181, 9821849, 985, and 12366) in contrast to ten protein structures (PDB IDs: 1IOB, 1MDI, 2Z63, 3BES, 5UC6, 1A02, 1H2K, 1TNF, 5F19, and 8TQD) given in table 2. Docking scores were associated across all protein–ligand combinations to classify promising candidates for further molecular simulation studies.

Table 2. Top 10 hub genes ranked by network analysis score

Rank	Gene symbol	Full name	Score
1	TNF	Tumor Necrosis Factor	2.98E+15
2	NFKB1	Nuclear Factor Kappa B Subunit 1	2.98E+15
3	HIF1A	Hypoxia Inducible Factor 1 Subunit Alpha	2.98E+15
4	PTGS2	Prostaglandin-Endoperoxide Synthase 2	2.98E+15
5	JUN	Jun Proto-Oncogene, AP-1 Transcription Factor Subunit	2.98E+15
6	IL1B	Interleukin 1 Beta	2.98E+15
7	IFNG	Interferon Gamma	2.98E+15
8	CASP3	Caspase 3	2.98E+15
9	IL1A	Interleukin 1 Alpha	2.93E+15
10	TLR4	Toll-Like Receptor 4	2.85E+15

Amongst the screened compounds, PubChem CID 12366 displayed the greatest favourable docking score against the protein structure 5F19 (−7.3 kcal/mol), indicating a comparatively favourable predicted binding interaction. The compound also showed moderate binding scores against other targets, including −6.0 kcal/mol against 1H2K and −5.5 kcal/mol against 3BES. Particularly, PubChem CID 9821849 displayed a docking score of −8.6 kcal/mol against 5F19, which was more favourable than that of CID 12366. Consequently, CID 9821849 was selected as the reference/control ligand for comparative molecular dynamics analysis, while CID 12366 was prioritized as the test compound all 10 target docked docking score exposed in supplementary table 4.

The docking results for 5F19 were particularly applicable to the successive simulation workflow because both the CID 12366–5F19 complex and the CID 9821849–5F19 control complex were advanced to molecular dynamics simulations. This paired analysis allowed comparison of their structural stability and interaction behaviour below simulated conditions. Overall, the docking results supported the selection of CID 12366 as the candidate ligand for further investigation, while CID 9821849 assisted as the comparator for appraising the relative behaviour of the two complexes.

The 2D and 3D interaction profiles of the 5F19–CID 12366 and 5F19–CID 9821849 complexes exposed distinct ligand–protein interaction patterns. The CID 12366 complex exhibited extensive van der Waals contacts involving residues such as GLY526, LEU384, TRP387, PHE381, and TYR385, alongside multiple π-alkyl interactions involving VAL523, PHE518, MET522, ILE377, PHE209, and VAL228. The reported π-alkyl interaction distances ranged from 3.98 to 5.88 Å presented in table 3. In comparison, CID 9821849 formed van der Waals contacts with TRP100, ILE112, LEU93, SER119, and ARG120, as well as π-alkyl interactions involving VAL89, VAL116, and TYR115, with distances ranging from 3.93 to 5.40 Å. These observations designate differences in the interaction patterns of the two ligands within their respective binding sites. However, the residue numbering varies considerably between the complexes, so the contacts should be interpreted in the context of the corresponding protein structure and binding pocket shown in fig 5.

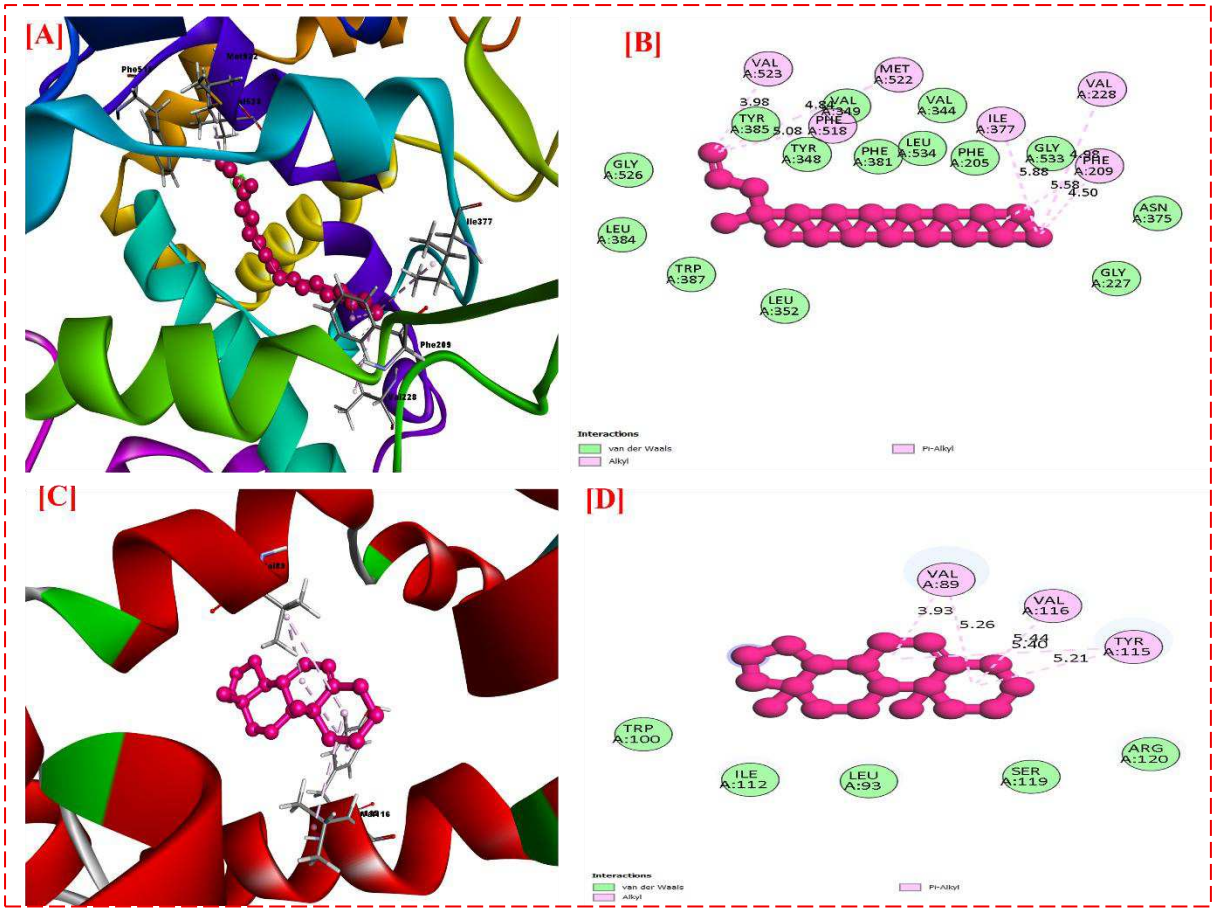


Figure 5: Three-dimensional binding poses and two-dimensional ligand–protein interaction maps of the 5F19–CID 12366 and 5F19–CID 9821849 complexes. (A, B) 3D binding pose and 2D interaction profile of CID 12366; (C, D) 3D binding pose and 2D interaction profile of CID 9821849. Interactions include van der Waals and π-alkyl contacts.

Table 3: Binding interactions and intermolecular distances of CID 12366 and CID 9821849 within the 5F19 protein binding site, showing interacting amino acid residues and van der Waals and π-alkyl interactions.

Complexes	Ligand name	Interaction	Residues			In A◦ respectively
5F19_12366	**Ethyl hexadecanoate**	**Van der Waals**	GLY526, LEU352, GLY533, VAL344, TYP348, TYR385	LEU384, GLY227, PHE205, PHE381,	TRP387, ASN375, LEU534, VAL349,	NA

		π-Alkyl / Pi-Alkyl	VAL523, PHE518, MET522, ILE377, VAL228	PHE518, PHE209,	3.98,4.84, 5.08,5.88, 4.90, 5.58, 4.50
5F19_9821849	**Abiraterone acetate**	**Van der Waals**	TRP100, ILE112, LEU93, SER119, ARG120		
		π-Alkyl / Pi-Alkyl	VAL89, VAL116, TYR115		3.93, 5.40, 5.21

Root Mean Square Deviation (RMSD) Analysis

The root-mean-square deviation (RMSD) analysis was accomplished to estimate the structural stability of the protein–ligand complex (5F19_21366) in contrast with the control complex (5F19_Control) throughout the 200 ns molecular dynamics simulation. As shown in Fig. 6, the test complex (black curve) showed a moderately high initial RMSD, with fluctuations reaching approximately 14–15 nm, followed by a gradual decrease and stabilization at around 5.5–6.0 nm. In contrast, the control complex (red curve) maintained a substantially lower RMSD, predominantly around 0.4–0.7 nm, with irregular minor fluctuations throughout the simulation.

The reported RMSD values were 14.60722 nm for the test complex and 1.088671 nm for the control complex. Overall, the test complex displayed greater structural deviation than the control, whereas the control displayed relatively lower deviations. However, the black curve's sustained RMSD of approximately 5.5–6.0 nm is unusually high for a conventionally aligned protein backbone, so the trajectory fitting, periodic boundary condition correction, atom selection, and RMSD units should be confirmed before concluding that the test complex is structurally unstable.

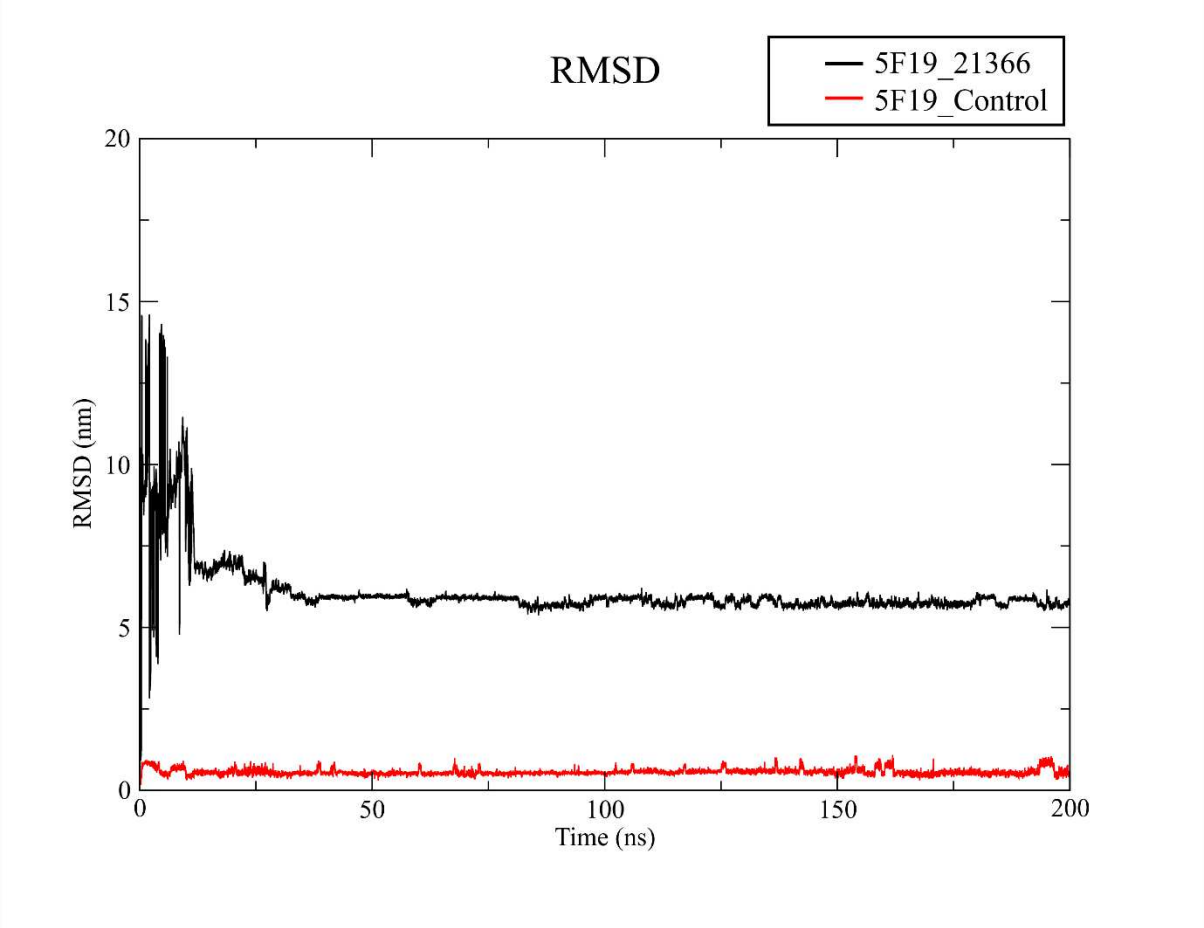


Figure 6. Root mean square deviation (RMSD) analysis of the 5F19–CID 12366 test complex and 5F19–CID 9821849 control complex during the 200-ns molecular dynamics simulation, illustrating changes in overall structural deviation over time.

RMSF Analysis

The root-mean-square fluctuation (RMSF) investigation was achieved to estimate residue-wise flexibility in the test complex and control during the 200 ns molecular dynamics simulation. As shown in Fig. 7, the test complex (red curve) exhibited greater fluctuations across several residues, with prominent peaks reaching approximately 0.66 nm, demonstrating regions of improved local flexibility. In assessment, the control complex (black curve) displayed comparatively lower fluctuations, predominantly around 0.05–0.20 nm, suggesting reduced residue-level flexibility (Chaudhary et al., 2026).

The average RMSF values were 0.3683 nm for the test complex and 0.119928 nm for the control, while the described maximum values were 0.6191 nm and 0.137164 nm, respectively. Overall, the control displayed lower residue-level fluctuations, whereas the test complex

presented greater local flexibility during the simulation. These differences may reflect variations in protein conformational dynamics upon ligand binding.

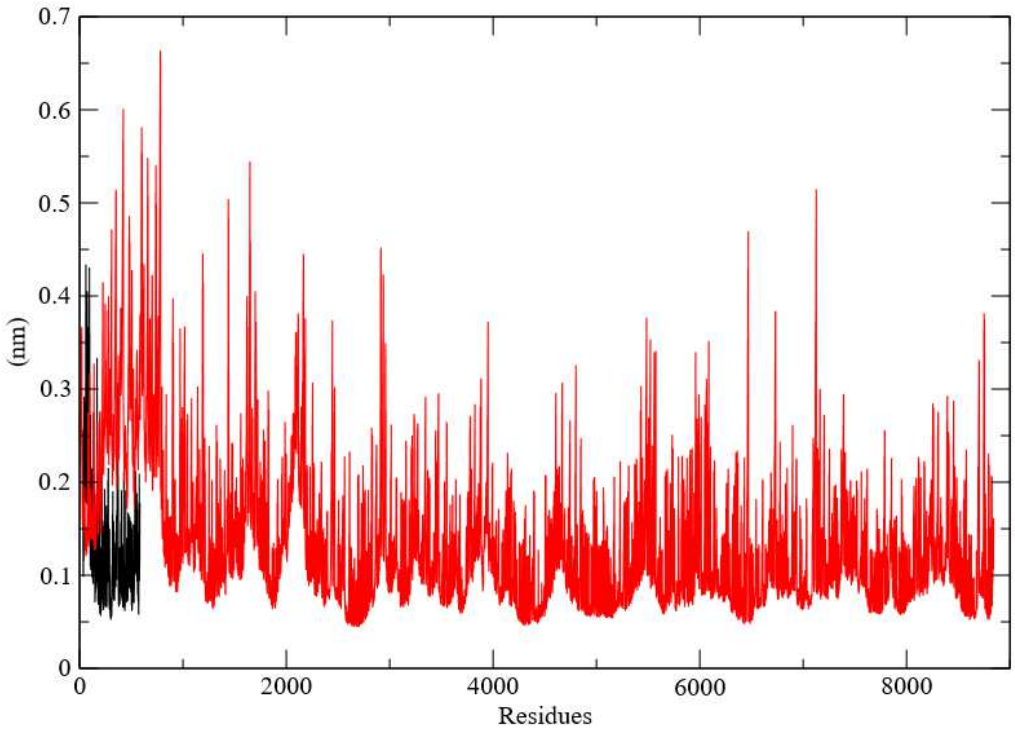


Figure 7. Root mean square fluctuation (RMSF) profiles of the 5F19–CID 12366 test complex and 5F19–CID 9821849 control complex, showing residue-wise fluctuations and local flexibility of the protein structure during the simulation.

Radius of Gyration (Rg) Analysis

The radius of gyration (Rg) was analysed to evaluate the compactness and structural stability of the protein–ligand complex throughout the 200 ns molecular dynamics simulation. As exposed in Fig. 8, both the test complex (5F19_21366, black curve) and the control complex (5F19_Control, red curve) exhibited comparatively stable Rg profiles, fluctuating predominantly between 2.44 and 2.50 nm. The test complex continued an average Rg of 2.062733 nm, whereas the control displayed an average value of 2.053852 nm, demonstrating broadly similar overall compactness based on the reported averages. The reported Rg ranges were 0.51498 nm for the test complex and 0.39202 nm for the control, suggesting greater variation in the test complex.

Overall, the Rg profiles designate that both systems maintained broadly similar structural compactness during the simulation, though the test complex showed somewhat greater fluctuations than the control. However, the reported average values do not match the approximately 2.45–2.50 nm values visible in the graph. The averages and ranges should therefore be recalculated or verified using the original GROMACS output before drawing a definitive conclusion.

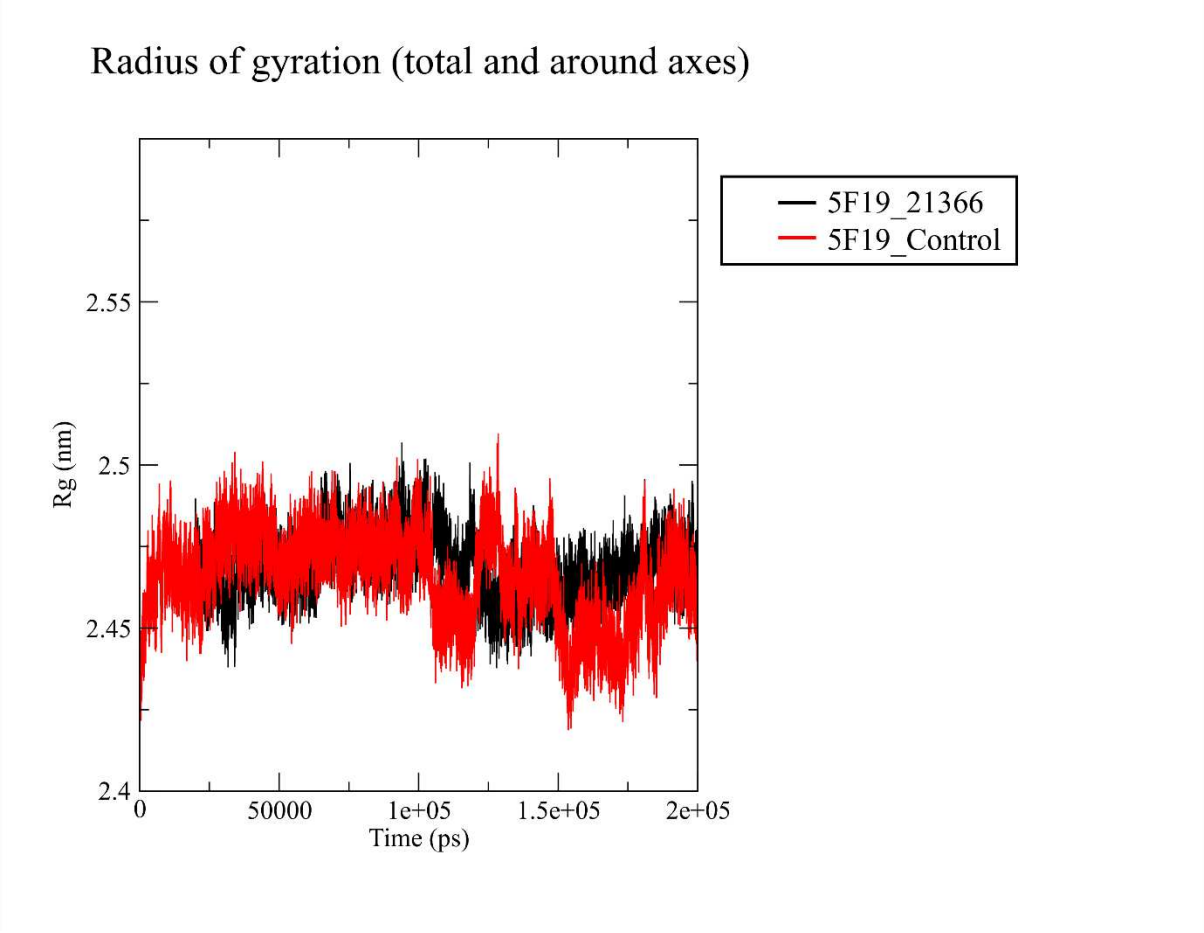


Figure 8. Radius of gyration (Rg) analysis of the 5F19–CID 12366 test complex and 5F19–CID 9821849 control complex over 200 ns, assessing changes in protein compactness and conformational organization.

Hydrogen Bond (H-bond) Analysis

Hydrogen-bond analysis was accomplished to appraise the persistence of intermolecular interactions between the protein and ligand throughout the 200 ns molecular dynamics simulation. As shown in Fig. 9, the test complex (5F19_21366, black curve) showed intermittent hydrogen-bond formation, with a maximum of approximately two hydrogen bonds

observed during the simulation. The control complex (5F19_Control, red curve) displayed no apparent hydrogen-bond formation in the displayed trajectory.

The reported average hydrogen-bond values were 0.067941 for the test complex and 0.006 for the control. These results suggest that the test complex formed hydrogen bonds more regularly than the control, potentially contributing to ligand–protein recognition and binding stability. However, hydrogen bonds were transient rather than continuously maintained throughout the simulation. Overall, the test complex displayed a higher average number of hydrogen bonds than the control, representing potentially stronger contributions from hydrogen-bond-mediated interactions. These discoveries should be interpreted alongside RMSD, RMSF, and radius of gyration analyses to obtain a comprehensive assessment of complex stability.

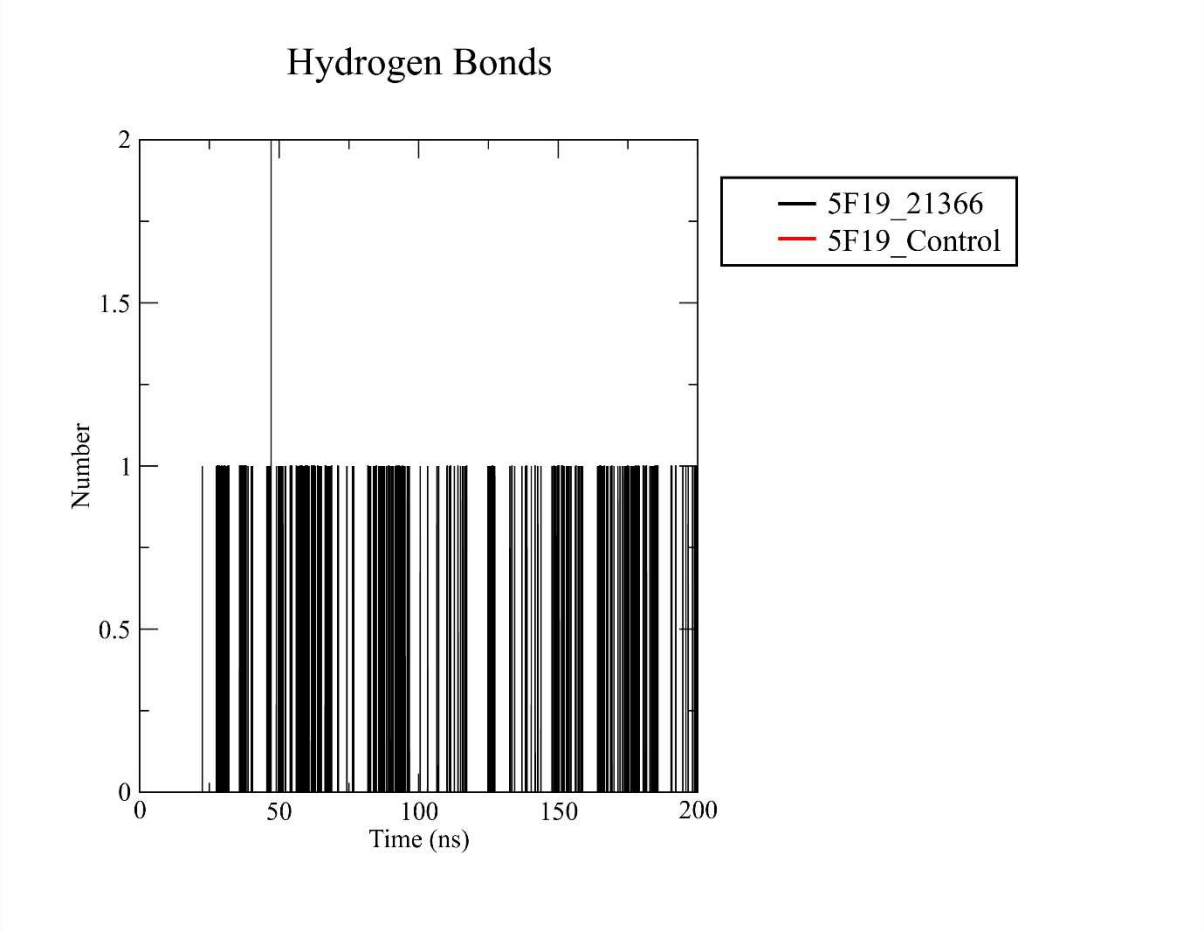


Figure 9. Hydrogen bond analysis of the 5F19–CID 12366 test complex and 5F19–CID 9821849 control complex throughout the 200-ns molecular dynamics simulation, illustrating the variation in the number of intermolecular hydrogen bonds over time.

Solvent Accessible Surface Area (SASA) Analysis

Solvent accessible surface area (SASA) analysis was accomplished to estimate changes in the solvent exposure of the protein–ligand complexes throughout the 200 ns molecular dynamics simulation. As shown in Fig. 10, both the test complex (5F19_21366, black curve) and the control complex (5F19_Control, red curve) exhibited fluctuations in SASA, predominantly within approximately 240–265 nm². The test complex displayed an average SASA of 251.2115 nm², while the control complex exhibited an average value of 250.9855 nm². The reported SASA ranges were 24.319 nm² and 33.5 nm² for the test and control complexes, respectively.

The comparable average SASA values recommend that both complexes maintained similar overall solvent exposure during the simulation. However, the control complex showed a broader informed range of fluctuations, whereas the test complex showed comparatively smaller variations. These discoveries suggest broadly similar solvent-exposure profiles, with potentially greater temporal variability in the control complex. Overall, the SASA results complement the RMSD, RMSF, and radius of gyration investigates in evaluating the structural behaviour of the simulated systems. The reported ranges should be substantiated against the original GROMACS output, as the visible graph spans approximately 230–270 nm², and the range values may not correspond to the full plotted trajectories.

The 200 ns molecular dynamics simulations provided insights into the structural dynamics of the test complex (5F19_21366) compared with the control (5F19_Control). RMSD and RMSF examines designated greater structural deviation and residue-level flexibility in the test complex, although the control displayed moderately lower fluctuations. In contrast, radius of gyration and SASA profiles suggested broadly comparable overall compactness and solvent exposure between the two systems. Hydrogen-bond analysis discovered more recurrent hydrogen-bond formation in the test complex than in the control, representing a potential involvement of these interactions to ligand–protein recognition. Cooperatively, these discoveries highlight differences in conformational dynamics and intermolecular interactions between the complexes. However, the unusually high reported RMSD for the test complex warrants verification of trajectory processing and units before drawing definitive conclusions regarding its stability shown in table 4.

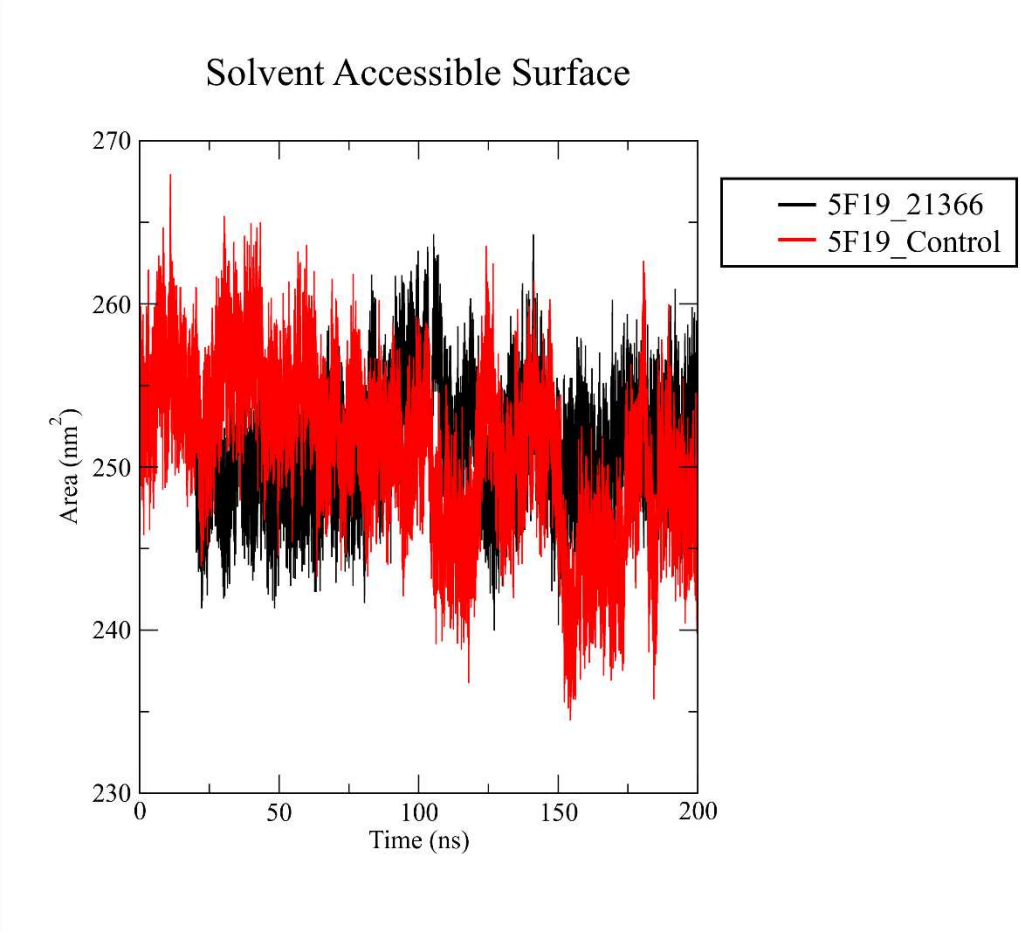


Figure 10. Solvent-accessible surface area (SASA) analysis of the 5F19–CID 12366 test complex and 5F19–CID 9821849 control complex during the 200-ns molecular dynamics simulation, evaluating changes in solvent exposure of the protein structure.

Table 4: Comparative molecular dynamics (MD) simulation parameters of the test complex (5F19_21366) and control complex (5F19_Control) over 200 ns, including root mean square deviation (RMSD), root mean square fluctuation (RMSF), radius of gyration (Rg), hydrogen bond formation (H-bond), and solvent-accessible surface area (SASA). The range and average values are reported for each parameter.

Complex	**RMSD**		**RMSF**		**ROG**		**H_bond**		**SASA**	
	Range (nm)	**Avg**	**Range (nm)**	**Avg**	**Range (nm)**	**Avg**	**Range (nm^2)**	**Avg**	**Range (nm^2)**	**Avg**

5F19_21366	14.60722	6.080645	0.3683	0.119928	0.5149 8	2.062 733	2	0.0679 41	24.31 9	251.2 115
5F19_Control	1.088671	0.561389	0.6191	0.137164	0.3920 2	2.053 852	1	0.006	33.5	250.9 855

3.6 External validation of core targets

mRNA Expression Levels of Core Targets

The mRNA expression levels of the top 10 hub genes were estimated in prostate cancer (PRAD) tissues and normal tissues using the expression profiles obtainable in Fig. 11. The results revealed differential expression patterns among the recognized essential targets. PTGS2 and TLR4 showed higher expression in normal tissues than in prostate cancer tissues, whereas TNF, NFKB1, HIF1A, JUN, IL1B, IFNG, CASP3, and IL1A exposed changing degrees of intersection between the two groups. PTGS2 demonstrated a statistically significant difference, as designated by the asterisk in the figure. These findings highlight the heterogeneous expression patterns of the selected hub genes and suggest their potential involvement in prostate cancer-associated biological processes. Further statistical validation is mandatory to establish the significance of expression differences for the remaining genes.

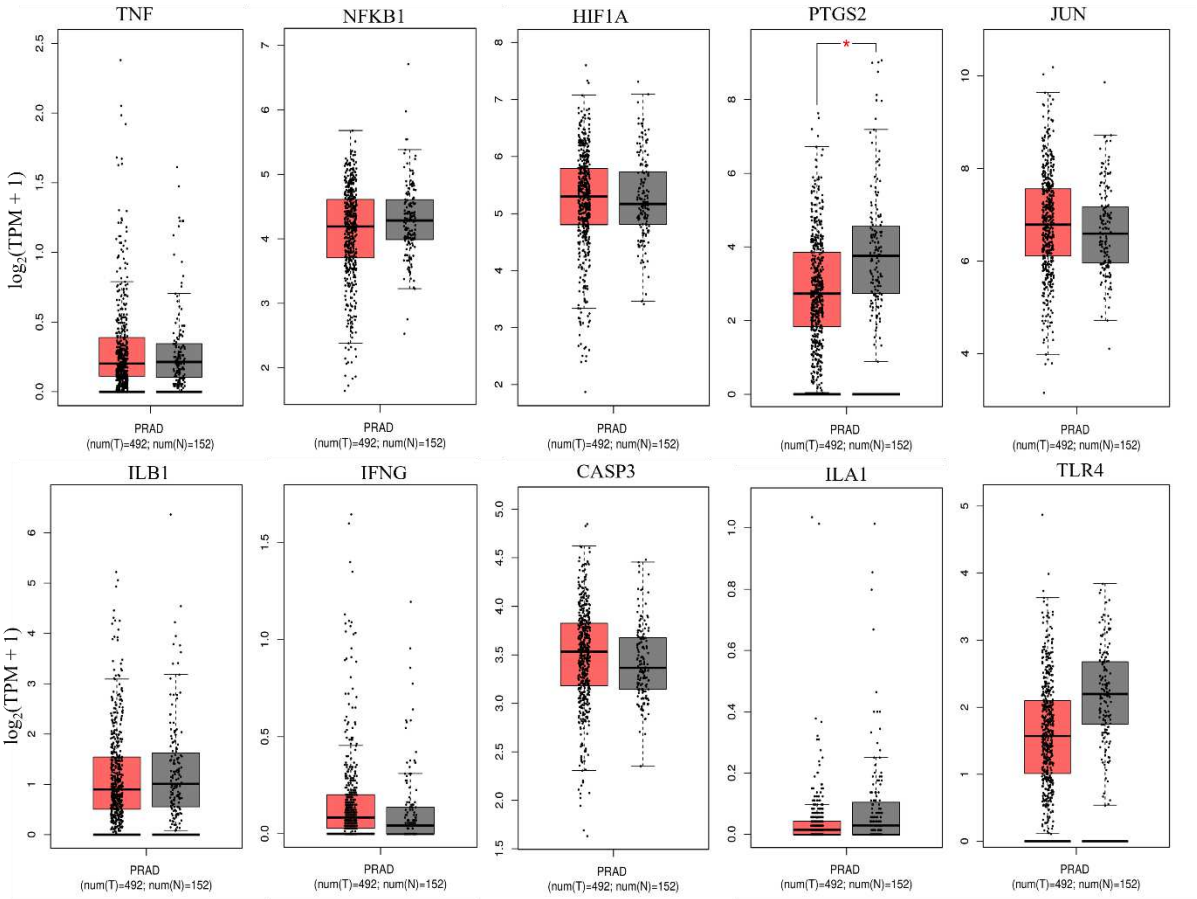


Figure 11: Differential expression analysis of prostate cancer-associated hub genes using the GEPIA2 database. Box plots compare gene expression levels between normal prostate tissues (green) and prostate adenocarcinoma tissues (red). (A) TNF; (B) NFKB1; (C) HIF1A; (D) PTGS2; (E) JUN; (F) IL1B; (G) IFNG; (H) CASP3; (I) IL1A; and (J) TLR4.

Prognostic significance of hub genes in prostate adenocarcinoma

The prognostic consequence of the ten hub genes was assessed using Kaplan–Meier survival analysis. As shown in Figure 12, PTGS2, JUN, CASP3, and TLR4 displayed statistically significant associations with overall survival (OS). Higher PTGS2 expression was accompanying with enhanced OS (HR = 0.55, 95% CI: 0.36–0.82, log-rank p = 0.0032). Likewise, high JUN expression was associated with a favourable survival outcome (HR = 0.65, 95% CI: 0.42–0.99, p = 0.045). In contrast, higher CASP3 expression was associated with poorer OS (HR = 1.81, 95% CI: 1.22–2.69, p = 0.0026). Higher TLR4 expression was associated with upgraded OS (HR = 0.44, 95% CI: 0.28–0.68, p = 0.00015).

The remaining genes—TNF (HR = 1.14, p = 0.57), NFKB1 (p > 0.05), HIF1A (HR = 0.71, p = 0.094), IL1B (HR = 1.20, p = 0.40), IFNG (HR = 1.61, p = 0.061), and IL1A (HR = 0.69, p = 0.081)—did not demonstrates statistically momentous associations with OS at the conservative p < 0.05 threshold. Overall, these discoveries suggest that PTGS2, JUN, CASP3, and TLR4 may have potential prognostic significance in prostate adenocarcinoma, though independent validation is needed.

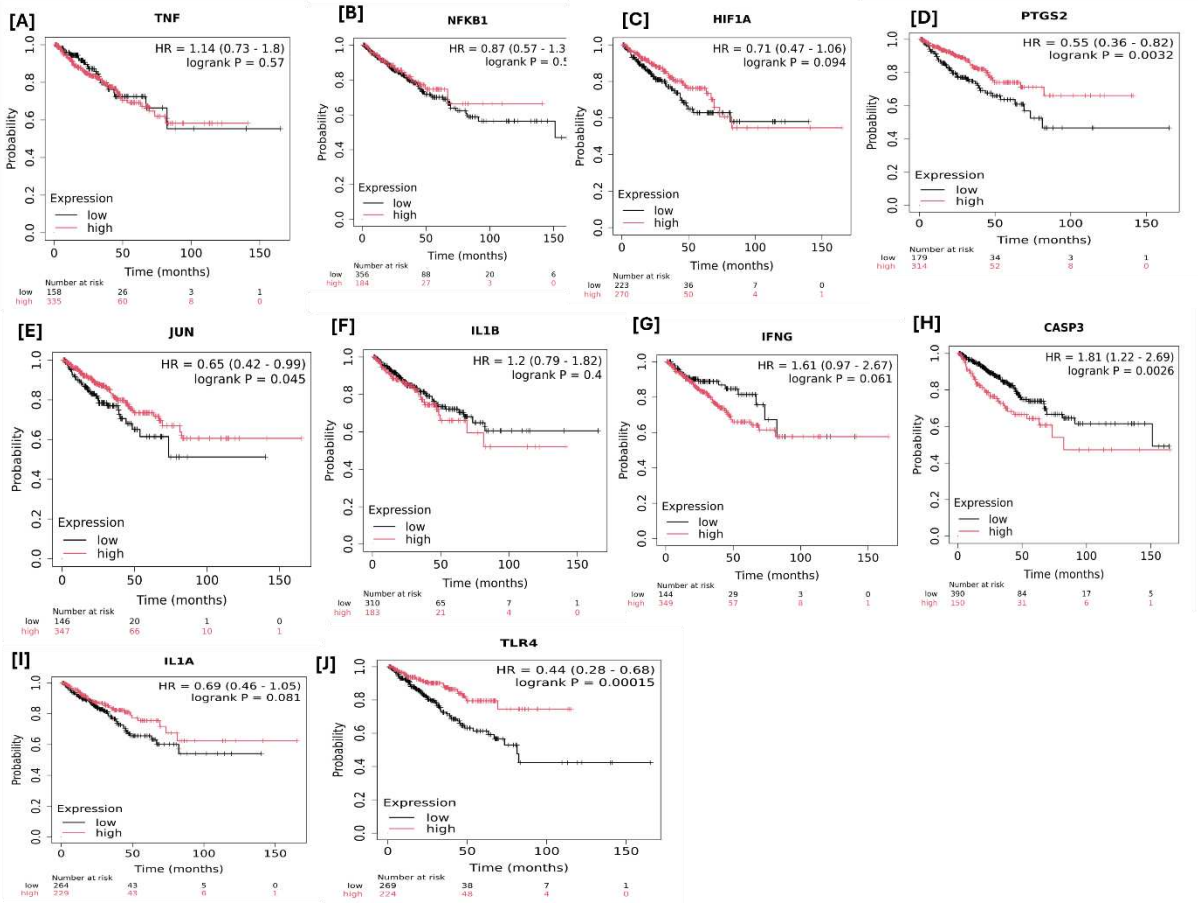


Figure 12. Kaplan–Meier overall survival analysis of the ten hub genes in prostate adenocarcinoma (PRAD). Survival curves compare patients with high (red) and low (black) expression of each hub gene. (A) TNF; (B) NFKB1; (C) HIF1A; (D) PTGS2; (E) JUN; (F) IL1B; (G) IFNG; (H) CASP3; (I) IL1A; and (J) TLR4. Hazard ratios (HRs), 95% confidence intervals (CIs), and log-rank p-values are displayed in the respective panels. p < 0.05 was considered statistically significant.

Promoter methylation analysis of hub genes in PRAD

Promoter methylation levels of the designated hub genes were evaluated using TCGA data by comparation normal prostate tissues (n = 50) with primary prostate tumour tissues (n = 502).

As exposed in the box plots, PTGS2 and IL1B displayed higher median promoter methylation levels in tumour tissues than in normal tissues. In contrast, TNF, JUN, IFNG, CASP3, and IL1A presented lower median methylation levels in primary tumours. NFKB1 and HIF1A displayed comparatively equivalent median methylation levels between the two groups, with modest differences in their distributions. These conclusions designate gene-specific variation in promoter methylation patterns in PRAD. TLR4 was not included in the displayed analysis; consequently, its promoter methylation status could not be measured. Statistical significance should be established using the corresponding p-values before drawing conclusions about differential methylation shown in figure 13.

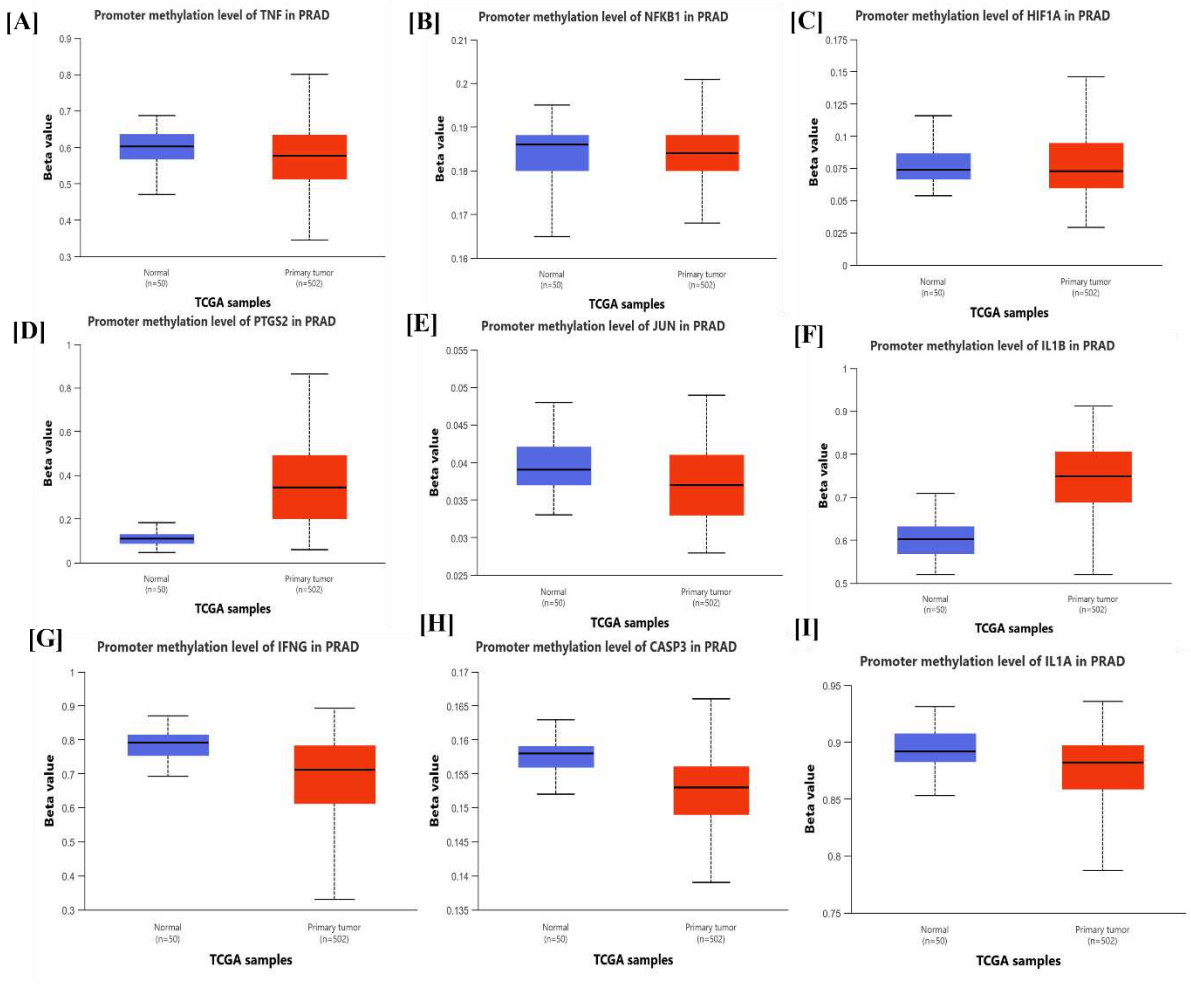


Figure 13. Promoter methylation profiles of hub genes in prostate adenocarcinoma (PRAD). Box plots compare promoter methylation beta values between normal prostate tissues (blue; n = 50) and primary prostate tumour tissues (red; n = 502) from TCGA. (A) TNF; (B) NFKB1; (C) HIF1A; (D) PTGS2; (E) JUN; (F) IL1B; (G) IFNG; (H) CASP3; and (I) IL1A. TLR4 was not available in the displayed figure. Beta values represent the degree of DNA methylation, with higher values indicating greater methylation.

Protein Expression Levels of Core Targets

Immunohistochemical (IHC) staining data from the Human Protein Atlas (HPA) database were surveyed to evaluate the protein expression patterns of the top 10 hub genes recognized in the prostate cancer (PRAD) PPI network. The staining images exposed variable protein expression patterns across the designated targets in prostate cancer and normal prostate tissues. Differences in staining intensity and distribution recommended heterogeneous expression profiles among the explored proteins. These explanations deliver complementary evidence for assessing the potential biological significance of the recognized hub genes in prostate cancer. However, the expression status of each target should be determined from its corresponding HPA annotations and matched tissue images. Where comparable IHC data were unavailable, the target was not involved in the proportional assessment (Fig. 14).

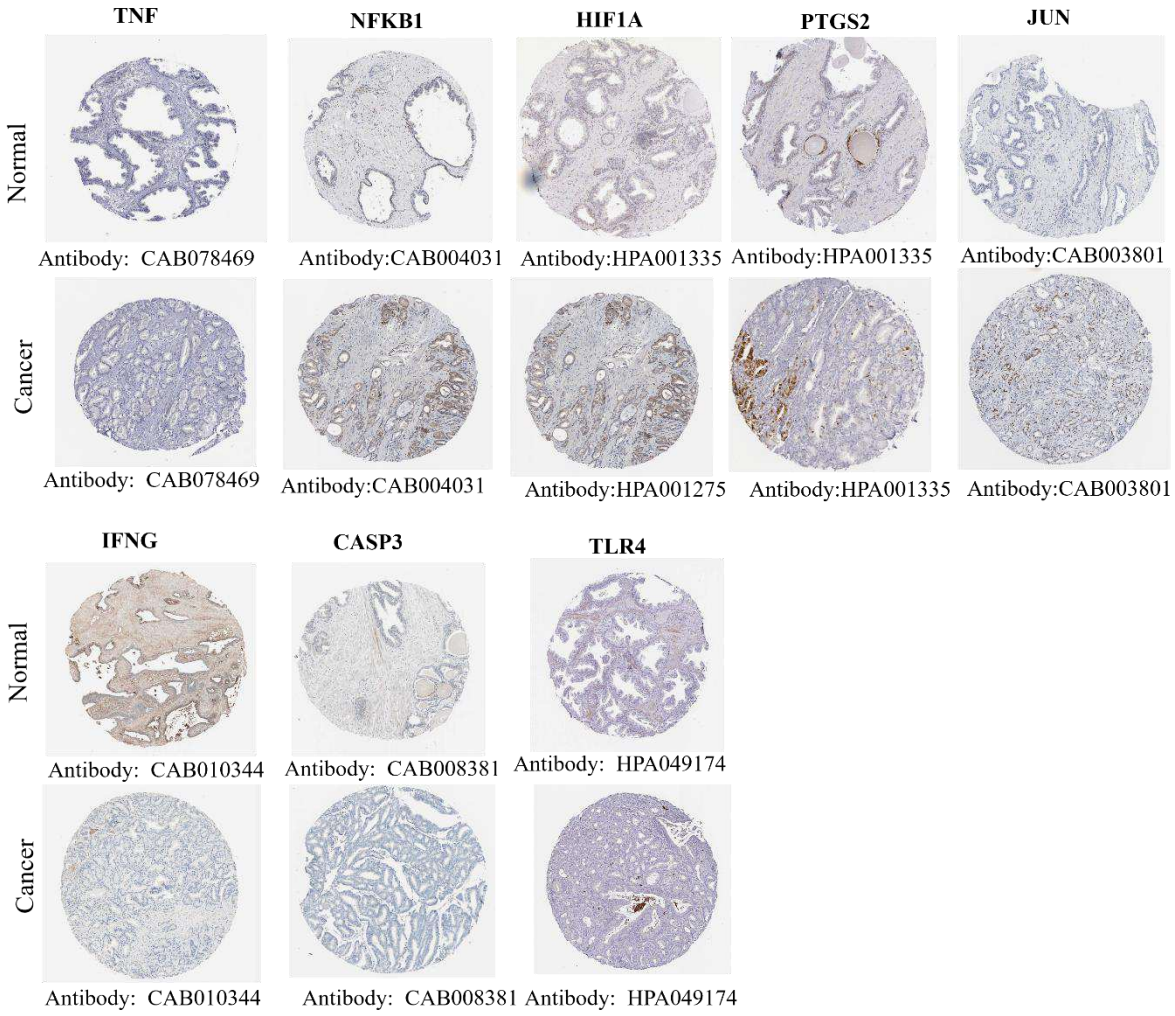


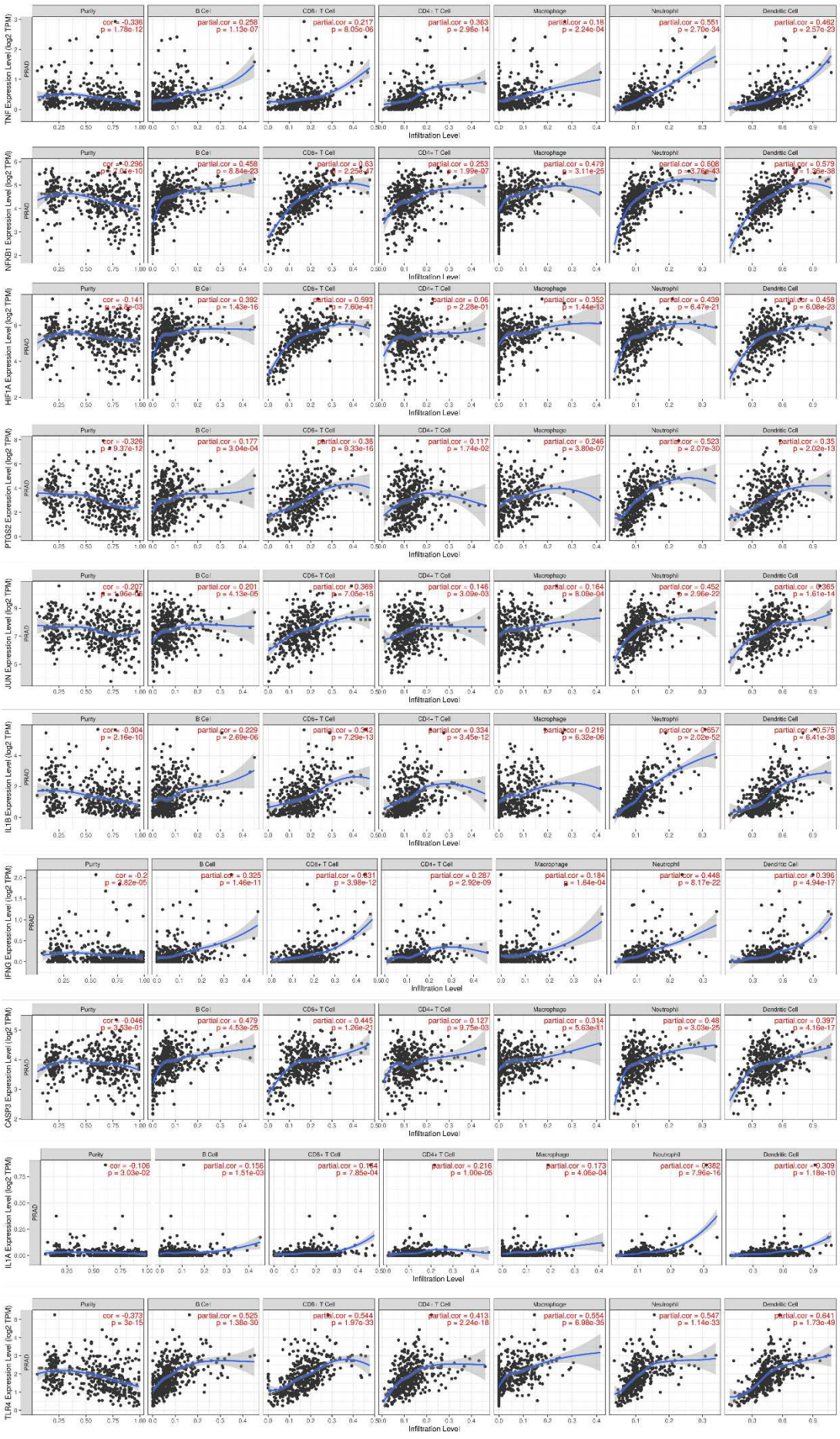
Figure 14: Immunohistochemical staining profiles of selected hub proteins in normal prostate and prostate cancer tissues obtained from the Human Protein Atlas database.

Immune Cell Infiltration of Core Targets

The relationship between the expression of the 10 core hub genes and immune cell infiltration in prostate adenocarcinoma (PRAD) was investigated using TIMER2.0. The analysis evaluated tumour purity and the assessed infiltration levels of B cells, $CD8^+$ T cells, $CD4^+$ T cells, macrophages, neutrophils, and dendritic cells (Fig. 15).

The results exposed principally negative associations between hub gene expression and tumour purity, while positive correlations were observed between most hub genes and immune cell infiltration. NFKB1, IL1B, IFNG, and TLR4 displayed principally strong positive associations with multiple immune cell populations. TLR4 expression was positively correlated with B cells (\(\rho=0.525\)), $CD8^+$ T cells (\(\rho=0.544\)), $CD4^+$ T cells (\(\rho=0.413\)), macrophages (\(\rho=0.554\)), neutrophils (\(\rho=0.547\)), and dendritic cells (\(\rho=0.641\)). Similarly, NFKB1 displayed positive correlations with $CD8^+$ T cells, neutrophils, dendritic cells, and other immune cell populations. TNF, PTGS2, and JUN also showed positive associations with several immune cell populations, predominantly neutrophils. HIF1A displayed positive correlations with B cells, $CD8^+$ T cells, macrophages, neutrophils, and dendritic cells, although its association with $CD4^+$ T cells appeared weak. CASP3 and IL1A presented generally weaker positive correlations with immune infiltration, while IL1A shown comparatively modest associations across most cell populations shown in table 5.

Overall, these findings suggest that the identified hub genes are associated with the immune microenvironment of PRAD, predominantly with the infiltration of neutrophils, dendritic cells, and T lymphocytes. These correlations deliver a basis for further investigation of the potential roles of the hub genes in tumour–immune interactions.


Purity
B Cell
CD8+ T Cell
CD4+ T Cell
Macrophage
Neutrophil
Dendritic Cell
TNF Expression Level (log2 TPM)
NFKB1 Expression Level (log2 TPM)
HIF1A Expression Level (log2 TPM)
PTGS2 Expression Level (log2 TPM)
JUN Expression Level (log2 TPM)
IL1B Expression Level (log2 TPM)
IFNG Expression Level (log2 TPM)
CASP3 Expression Level (log2 TPM)
IL1A Expression Level (log2 TPM)
TLR4 Expression Level (log2 TPM)
PRAD
Infiltration Level

641

Figure 15. TIMER2.0-based correlation analysis of the top 10 hub genes (TNF, NFKB1, HIF1A, PTGS2, JUN, IL1B, IFNG, CASP3, IL1A, and TLR4) with tumour purity and immune cell infiltration in prostate adenocarcinoma (PRAD). The scatter plots show partial correlation coefficients between gene expression and the estimated infiltration levels of B cells, $CD8^+$ T cells, $CD4^+$ T cells, macrophages, neutrophils, and dendritic cells. Red text indicates correlation coefficients and corresponding p-values.

Table 5. Correlation between core hub gene expression and immune cell infiltration in PRAD

Hub gene	Tumour purity	B cells	$CD8^+$ T cells	$CD4^+$ T cells	Macrophages	Neutrophils	Dendritic cells
TNF	−0.336	+0.258	+0.217	+0.363	+0.180	+0.551	+0.462
NFKB1	−0.296	+0.458	+0.630	+0.253	+0.479	+0.608	+0.579
HIF1A	−0.141	+0.392	+0.593	+0.060	+0.352	+0.439	+0.458
PTGS2	−0.326	+0.177	+0.380	+0.117	+0.246	+0.523	+0.350
JUN	−0.207	+0.201	+0.369	+0.146	+0.164	+0.452	+0.365
IL1B	−0.304	+0.229	+0.342	+0.334	+0.219	+0.657	+0.575
IFNG	−0.200	+0.325	+0.631	+0.287	+0.184	+0.448	+0.396
CASP3	−0.046	+0.479	+0.445	+0.127	+0.314	+0.480	+0.397
IL1A	−0.106	+0.156	+0.164	+0.216	+0.173	+0.382	+0.309
TLR4	−0.373	+0.525	+0.544	+0.413	+0.554	+0.547	+0.641

Discussion

The present study employed an combined computational framework to investigate the potential anticancer significance of *Moringa oleifera*-derived bioactive compounds against prostate cancer (PCa). The identification of 253 overlapping targets between compound-associated predictions and PCa-related genes recommends probable molecular associations between the

selected phytochemicals and disease-associated biological networks. PPI investigation additional acknowledged a highly interconnected functional module, with TNF, NFKB1, HIF1A, PTGS2, JUN, IL1B, IFNG, CASP3, IL1A, and TLR4 developing as the top-ranked hub genes. Their functional enrichment implicated inflammation, apoptosis, oxidative stress, immune regulation, and cancer-associated signalling, highlighting the interconnected nature of these procedures in prostate cancer biology.

Molecular docking recognized CID 9821849 as having a more favourable predicted binding score against the 5F19 structure (−8.6 kcal/mol) than CID 12366 (−7.3 kcal/mol). CID 12366 was nevertheless designated for further investigation together with the reference ligand. The experimental van der Waals and π-alkyl interactions designate different prophesied binding patterns; however, docking scores alone cannot establish binding affinity or biological activity. The 200-ns MD simulations exposed differences in structural deviation, residue flexibility, and hydrogen-bond formation between the test and control complexes, whereas their described radius of gyration and solvent-accessible surface area profiles recommended broadly comparable compactness and solvent exposure. The remarkably high RMSD described for the test complex necessitates verification of trajectory alignment, periodic-boundary correction, and units before firm conclusions about its constancy can be drawn (Maurya et al., 2026).

External analyses providing additional biological context for the prioritized targets. Survival analysis recognized important associations between PTGS2, JUN, CASP3, and TLR4 expression and overall survival, while immune-infiltration analysis designated associations between several hub genes and immune-cell populations in prostate adenocarcinoma. Gene-expression and promoter-methylation examines also exposed heterogeneous patterns across the selected targets. These discoveries propose that the recognized genes warrant further investigation in PCa; nevertheless, experimental associations do not establish causal roles or establish that the selected compounds moderate these targets.

Overall, the major contribution of this study is the integration of phytochemical prioritization, network pharmacology, molecular docking, MD simulations, and external molecular and experimental data analysis (Maurya et al., 2026). This workflow delivers a basis for ranking candidate compounds and inspecting their potential molecular significance to prostate cancer. Further experimental studies, including direct binding assays, prostate cancer cell-based validation, and pharmacological evaluation, are obligatory to establish their mechanisms of action, efficacy, and safety.

Conclusion

This study integrates network pharmacology, molecular docking, 200-ns molecular dynamics simulations, and multi-level molecular and clinical data analyses to prioritize *Moringa oleifera*-derived compounds and potential targets accompanying with prostate cancer. The discoveries highlight interrelated inflammatory, apoptotic, and immune-related networks and deliver preliminary insights into ligand–protein interactions. This integrated computational background proposals a basis for candidate prioritization; however, experimental validation, confirmation of RMSD results, binding free-energy calculations, and in vitro and in vivo studies are mandatory to establish molecular mechanisms, anticancer efficacy, and safety. Future research should authorize the prioritized compounds and targets to advance their potential translational significance in prostate cancer.

References:

1. Ahmed, M. M., Tazyeen, S., Ali, R., Alam, A., Imam, N., Malik, M. Z., Ali, S., & Ishrat, R. (2022). Network centrality approaches used to uncover and classify most influential nodes with their related miRNAs in cardiovascular diseases. *Gene Reports*, *27*, 101555. https://www.sciencedirect.com/science/article/pii/S2452014422000632
2. Ahmed, W., Wang, Y., Ji, W., Liu, S., Zhou, S., Pan, J., Li, Z., Wang, F., & Wang, X. (2025). Unraveling the mechanism of the endophytic bacterial strain pseudomonas oryzihabitans GDW1 in enhancing tomato plant growth through modulation of the host transcriptome and bacteriome. *International Journal of Molecular Sciences*, *26*(5), 1922. https://www.mdpi.com/1422-0067/26/5/1922
3. Bader, G. D., & Hogue, C. W. (2003). An automated method for finding molecular complexes in large protein interaction networks. *BMC Bioinformatics*, *4*(1), 2. https://doi.org/10.1186/1471-2105-4-2
4. Bayram, E., Broggi, G., & Ayan, D. (2026). Integrative Bioinformatic Characterization of the HDAC6-Driven Cytoskeleton–Wnt Signaling Interface in Hepatocellular Carcinoma: Implications for Immune Modulation and Therapeutic Targeting. *International Journal of Molecular Sciences*, *27*(12), 5201. https://www.mdpi.com/1422-0067/27/12/5201
5. Botstein, D., Cherry, J. M., Ashburner, M., Ball, C. A., Blake, J. A., Butler, H., Davis, A. P., Dolinski, K., Dwight, S. S., & Eppig, J. T. (2000). Gene Ontology: Tool for the unification of biology. *Nat Genet*, *25*(1), 25–29. https://www.academia.edu/download/47188709/Gene_ontology_tool_for_the_unification_o20160712-16194-16cpcbf.pdf
6. Bouamri, L. E., Laaouina, S., Lakrim, I., Nour, H., Yamari, I., Samadi, A., Bouachrine, M., & Chtita, S. (2026). Integrated Computational Investigation of Cannabis sativa Phytoconstituents as Putative Multi-Target Inhibitors in Skin Cancer: A Molecular Docking, Dynamics, and ADMET Profiling Study. *Pharmaceuticals*, *19*(2), 315. https://www.mdpi.com/1424-8247/19/2/315
7. Chaudhary, A., Banerjee, S., Shukla, P., Ehsan, S., & Singh, M. P. (2026). Comparative analysis of antibacterial and antioxidant properties as well as phytochemical compositions of Moringa oleifera gum, flower, and fruit and Elaeocarpus augustifolius

leaf and bark, synergistic with Pleurotus membranaceus. *International Microbiology*, *29*(5), 663–684. https://doi.org/10.1007/s10123-026-00805-4

8. Chaudhary, A., Ehsan, S., Maurya, S., Yadav, S., & Singh, M. P. (2026). Antioxidant and antibacterial potency of Pleurotus citrinopileatus: By GC–MS characterization, bioactive compound profiling, synergy analysis, and In-Silico validation of microbial target interactions. *Folia Microbiologica*. https://doi.org/10.1007/s12223-026-01555-6
9. Chin, C.-H., Chen, S.-H., Wu, H.-H., Ho, C.-W., Ko, M.-T., & Lin, C.-Y. (2014). cytoHubba: Identifying hub objects and sub-networks from complex interactome. *BMC Systems Biology*, *8*(S4), S11. https://doi.org/10.1186/1752-0509-8-S4-S11
10. Deng, X., Wang, Y., Guo, H., Wang, Q., Rao, S., & Wu, H. (2023). Pan-cancer analysis and experimental validation of SOX4 as a potential diagnosis, prognosis, and immunotherapy biomarker. *Cancers*, *15*(21), 5235. https://www.mdpi.com/2072-6694/15/21/5235
11. Desai, M., Singh, S. D., Nagamani, S., Malik, S., Singh, A., Kukreti, R., Kukreti, S., & Grewal, G. K. (2025). Decoding the relationship between oxidative stress and antiseizure medications using network pharmacology and molecular docking. *Scientific Reports*, *15*(1), 33294. https://www.nature.com/articles/s41598-025-02884-1
12. Divya, S., Pandey, V. K., Dixit, R., Rustagi, S., Suthar, T., Atuahene, D., Nagy, V., Ungai, D., Ahmed, A. E. M., & Kovács, B. (2024). Exploring the phytochemical, pharmacological and nutritional properties of Moringa oleifera: A comprehensive review. *Nutrients*, *16*(19), 3423. https://www.mdpi.com/2072-6643/16/19/3423
13. Du, J., Yuan, Z., Ma, Z., Song, J., Xie, X., & Chen, Y. (2014). KEGG-PATH: Kyoto encyclopedia of genes and genomes-based pathway analysis using a path analysis model. *Molecular BioSystems*, *10*(9), 2441–2447. https://academic.oup.com/molecular-omics/article-abstract/10/9/2441/8323951
14. Ehsan, S., Chaudhary, A., Maurya, S., Mishra, D., & Singh, M. P. (2026). *Identification of crucial genes and biological pathways in lung adenocarcinoma by network pharmacology, molecular docking, and simulation studies*. https://assets-eu.researchsquare.com/files/rs-9147467/v1_covered_dd6107a2-441a-4eea-8a03-8182a387e79d.pdf
15. Ehsan, S., Mishra, D., Chaudhary, A., Maurya, S., Gaur, A., Shanker, R., & Singh, M. P. (2026). Integrated in silico and experimental evaluation of ergosterol from Pleurotus membranaceus against lung cancer. *Discover Chemistry*, *3*(1), 410. https://doi.org/10.1007/s44371-026-00871-7
16. Gao, Y., Hu, Y., Zhu, Y., Gao, X., Hao, W., Chen, X., & Zheng, Z. (2025). Pan-cancer analysis reveals netrin-1 receptors as potential tumor biomarkers and immune-related therapeutic targets. *Scientific Reports*, *15*(1), 44015. https://www.nature.com/articles/s41598-025-28437-0
17. Grewal, S., Deswal, G., Grewal, A. S., & Guarve, K. (2025). Molecular dynamics simulations: Insights into protein and protein ligand interactions. *Advances in Pharmacology*, *103*, 139–162. https://www.sciencedirect.com/science/article/pii/S1054358925000079
18. Gupta, N., More, R., Singh, J., Parida, B. P., Anand, A., & Tiwari, A. (2026). *LC-HRMS-based phytochemical profiling of the ethanolic extract of Moringa oleifera seeds against toxic hepatotoxicity supported by in silico network design, molecular docking and simulation studies*. https://assets-eu.researchsquare.com/files/rs-8794547/v1/c2ab8c8c-b0e0-43d1-9ffe-f0bc7b891bb5.pdf
19. Harris, W. P., Mostaghel, E. A., Nelson, P. S., & Montgomery, B. (2009). Androgen deprivation therapy: Progress in understanding mechanisms of resistance and

optimizing androgen depletion. *Nature Clinical Practice Urology*, *6*(2), 76–85. https://www.nature.com/articles/ncpuro1296

20. Hazarika, S., Lal, M., Rahaman, S. B., Debnath, U., & Rawal, R. K. (2025). Computational screening of moringa oleifera compounds for immunomodulatory targets: Identification and validation of core genes. *South African Journal of Botany*, *185*, 331–347. https://www.sciencedirect.com/science/article/pii/S0254629925004478
21. He, Q., Liu, C., Wang, X., Rong, K., Zhu, M., Duan, L., Zheng, P., & Mi, Y. (2023). Exploring the mechanism of curcumin in the treatment of colon cancer based on network pharmacology and molecular docking. *Frontiers in Pharmacology*, *14*, 1102581. https://www.frontiersin.org/journals/pharmacology/articles/10.3389/fphar.2023.1102581/full
22. Hou, F., Yu, Z., Cheng, Y., Liu, Y., Liang, S., & Zhang, F. (2022). Deciphering the pharmacological mechanisms of Scutellaria baicalensis Georgi on oral leukoplakia by combining network pharmacology, molecular docking and experimental evaluations. *Phytomedicine*, *103*, 154195. https://www.sciencedirect.com/science/article/pii/S0944711322002732
23. Jia, Y., Gong, M., & Ke, Z. (2024). The Pharmacological Mechanisms Underlying the Protective Effect of Ginsenoside Rg3 against Heart Failure. *Cardiology Research and Practice*, *2024*(1), 3373410. https://doi.org/10.1155/2024/3373410
24. Khanal, P., Chikhale, R., Dey, Y. N., Pasha, I., Chand, S., Gurav, N., Ayyanar, M., Patil, B. M., & Gurav, S. (2022). Withanolides from *Withania somnifera* as an immunity booster and their therapeutic options against COVID-19. *Journal of Biomolecular Structure and Dynamics*, *40*(12), 5295–5308. https://doi.org/10.1080/07391102.2020.1869588
25. Kumar, R., Tripathi, R., Sinha, N. R., & Mohan, R. R. (2024). Transcriptomic landscape of quiescent and proliferating human corneal stromal fibroblasts. *Experimental Eye Research*, *248*, 110073. https://www.sciencedirect.com/science/article/pii/S001448352400294X
26. Li, B., Zhao, X., Ding, Y., & Zhang, Y. (2025). Network toxicology and molecular docking to investigate the mechanism of bisphenol A toxicity in human diabetic cardiomyopathy. *Ecotoxicology and Environmental Safety*, *299*, 118301. https://www.sciencedirect.com/science/article/pii/S0147651325006372
27. Liu, K., Chen, Y., Feng, P., Wang, Y., Sun, M., Song, T., Tan, J., Li, C., Liu, S., & Kong, Q. (2022a). Identification of pathologic and prognostic genes in prostate cancer based on database mining. *Frontiers in Genetics*, *13*, 854531. https://www.frontiersin.org/journals/genetics/articles/10.3389/fgene.2022.854531/full
28. Liu, K., Chen, Y., Feng, P., Wang, Y., Sun, M., Song, T., Tan, J., Li, C., Liu, S., & Kong, Q. (2022b). Identification of pathologic and prognostic genes in prostate cancer based on database mining. *Frontiers in Genetics*, *13*, 854531. https://www.frontiersin.org/journals/genetics/articles/10.3389/fgene.2022.854531/full
29. Long, X., Hou, H., Wang, X., Liu, S., Diao, T., Lai, S., Hu, M., Zhang, S., Liu, M., & Zhang, H. (2020). Immune signature driven by ADT-induced immune microenvironment remodeling in prostate cancer is correlated with recurrence-free survival and immune infiltration. *Cell Death & Disease*, *11*(9), 779. https://www.nature.com/articles/s41419-020-02973-1
30. Maurya, S., Ehsan, S., Chaudhary, A., Yadav, S., & Singh, M. P. (2026). Integrated in silico pharmacology of Pleurotus ostreatus-derived bioactive compounds targeting EGFR using network pharmacology and molecular. *In Silico Pharmacology*, *14*(2), 188. https://doi.org/10.1007/s40203-026-00690-9

31. Maurya, S., Shanker, R., Shukla, A. K., Ehsan, S., & Singh, M. P. (2026). Computational evaluation of anticancer potential of Pleurotus sajor- caju derived bioactive compounds against breast cancer targets using virtual screening. *Discover Chemistry*, *3*(1), 309. https://doi.org/10.1007/s44371-026-00761-y
32. Militaru, F. C., Militaru, V., Crisan, N., Bocsan, I. C., Udrea, A. A., Catana, A., Kutasi, E., & Militaru, M. S. (2023). Molecular basis and therapeutic targets in prostate cancer: A comprehensive review. *Biomolecules and Biomedicine*, *23*(5), 760. https://pmc.ncbi.nlm.nih.gov/articles/PMC10494850/
33. Muazzam, A. (2021). *Identification of prostate cancer biomarkers for diagnosis and stratification of disease*. The University of Manchester (United Kingdom). https://search.proquest.com/openview/f5f399968b3a194704ecc76dc564695d/1?pq-origsite=gscholar&cbl=2026366&diss=y
34. Nagy, Á., Munkácsy, G., & Gy\Horffy, B. (2021). Pancancer survival analysis of cancer hallmark genes. *Scientific Reports*, *11*(1), 6047. https://www.nature.com/articles/s41598-021-84787-5
35. Nivatya, H. K., Singh, A., Kumar, N., Sonam, Sharma, L., Singh, V., Mishra, R., Gaur, N., & Mishra, A. K. (2025). Assessing molecular docking tools: Understanding drug discovery and design. *Future Journal of Pharmaceutical Sciences*, *11*(1), 111. https://doi.org/10.1186/s43094-025-00862-y
36. Rajadnya, R., Sharma, N., Mahajan, A., Ulhe, A., Patil, R., Hegde, M., & Mali, A. (2024). Novel systems biology experimental pipeline reveals matairesinol's antimetastatic potential in prostate cancer: An integrated approach of network pharmacology, bioinformatics, and experimental validation. *Briefings in Bioinformatics*, *25*(5), bbae466. https://academic.oup.com/bib/article-abstract/25/5/bbae466/7761958
37. Rombolà, L., Scuteri, D., Marilisa, S., Watanabe, C., Morrone, L. A., Bagetta, G., & Corasaniti, M. T. (2020). Pharmacokinetic interactions between herbal medicines and drugs: Their mechanisms and clinical relevance. *Life*, *10*(7), 106. https://www.mdpi.com/2075-1729/10/7/106
38. Salmaso, V., & Moro, S. (2018). Bridging molecular docking to molecular dynamics in exploring ligand-protein recognition process: An overview. *Frontiers in Pharmacology*, *9*, 923. https://www.frontiersin.org/journals/pharmacology/articles/10.3389/fphar.2018.00923/full
39. Shannon, P., Markiel, A., Ozier, O., Baliga, N. S., Wang, J. T., Ramage, D., Amin, N., Schwikowski, B., & Ideker, T. (2003). Cytoscape: A software environment for integrated models of biomolecular interaction networks. *Genome Research*, *13*(11), 2498–2504. https://genome.cshlp.org/content/13/11/2498
40. Sharma, A., Sharma, A., Maheshwari, D. K., Kumar, S., & Sharma, A. K. (2025). Integrated network pharmacology and molecular docking reveal therapeutic potential of Moringa oleifera glycosides, targeting key regulatory genes in colorectal cancer. *In Silico Pharmacology*, *13*(3), 166. https://doi.org/10.1007/s40203-025-00461-y
41. Singh, A., Ohri, D., Wolkenhauer, O., Gautam, N. K., Gupta, S., & Singh, K. P. (2025). Exploring the Therapeutic Potential of Moringa oleifera Against Lung Cancer Through Network Modeling and Molecular Docking Analysis. *International Journal of Molecular Sciences*, *26*(20), 10191. https://www.mdpi.com/1422-0067/26/20/10191
42. Szklarczyk, D., Nastou, K., Koutrouli, M., Kirsch, R., Mehryary, F., Hachilif, R., Hu, D., Peluso, M. E., Huang, Q., & Fang, T. (2025). The STRING database in 2025: Protein networks with directionality of regulation. *Nucleic Acids Research*, *53*(D1), D730–D737. https://academic.oup.com/nar/article-abstract/53/D1/D730/7903368

43. Xu, H., Qiu, W., Zhu, C., Zhao, N., & Sha, J. (2026). Network pharmacology and bioinformatics analysis–based strategy for exploring the mechanisms of luteolin in the treatment of five types of cancer: A retrospective computational study. *Journal of International Medical Research*, *54*(6), 03000605261460317. https://doi.org/10.1177/03000605261460317
44. Yadav, A. J., & Padhi, A. K. (2025). Synergizing multiresolution simulations, interface redesign, and hotspot mapping to decipher pathogenic mutation-driven structural modulation in VCP. *Computers in Biology and Medicine*, *194*, 110560. https://www.sciencedirect.com/science/article/pii/S0010482525009114
45. Zhong, Z., Guo, X., & Zheng, Y. (2022). Network Pharmacology-Based and Molecular Docking Analysis of Resveratrol'sPharmacological Effects on Type I Endometrial Cancer. *Anti-Cancer Agents in Medicinal Chemistry*, *22*(10), 1933–1944. https://doi.org/10.2174/1871520621666211015140455